Constraining an Early Matter-Dominated Era through Cosmological Simulations

By
Sheridan Beckwith Green

Senior Honors Thesis
Department of Physics and Astronomy
University of North Carolina at Chapel Hill

April 28, 2017

Approved:

Adrienne Erickcek

Prof. Adrienne Erickcek, Thesis Advisor

Prof. Charles Evans, Reader

Prof. Louise Dolan, Reader

Abstract

An early matter-dominated era (EMDE) is a brief period between the end of inflation and reheating where a matter-like energy source dominates the cosmic stage. During the EMDE, sub-horizon matter density perturbations grow linearly with the scale factor, as compared to logarithmically during the radiation-dominated (RD) era. Perturbation modes outside the comoving Hubble horizon at reheating, with $R > R_H \equiv 1/(a_{\rm RH}H_{\rm RH})$ and thus $k < k_{\rm RH}$, are unaffected by the EMDE. Free-streaming of the dark matter particle will eliminate structure formation on scales below the free-streaming cut-off scale $R_{cut} = 1/k_{\rm cut}$. Modes in the wavenumber range $k_{\rm RH} < k < k_{\rm cut}$ will be enhanced by the EMDE, and thus we are interested in the ratio $k_{\rm cut}/k_{\rm RH}$ as a function of the reheat temperature $T_{\rm RH}$, temperature at kinetic decoupling in a RD universe $T_{\rm kdS}$, and dark matter mass m_χ. A larger ratio corresponds to a larger range of modes enhanced by the EMDE. We find that for a ratio $T_{\rm kdS}/T_{\rm RH} \approx 6$, a ratio $k_{\rm cut}/k_{\rm RH} = 20$ is attainable. The enhanced matter power spectrum is used as initial conditions for the `GADGET-2` N-body simulation code to study the formation and survival fraction of dark matter microhalos below the reheat mass. The microhalos that survive until today are bound into galaxy-mass host halos as substructure. This high-density substructure causes a boost in the dark matter annihilation rate. Our simulation results demonstrate that slightly fewer microhalos survive than previously expected, resulting in a somewhat lower annihilation boost factor than that of analytical predictions.

CONTENTS

I. INTRODUCTION

The first second of the Universe is the most poorly understood epoch on the cosmological timeline. There is strong evidence that a rapid accelerating expansion of space, known as cosmic inflation, lasted from $\sim 10^{-36}$ to $\sim 10^{-32}$ seconds after the Big Bang [1]. The current cosmological model splits the post-inflation history of the universe into the eras of radiation, matter, and dark energy domination. The inflationary period rapidly decreases radiation density and yet the universe must become radiation dominated before the onset of Big Bang Nucleosynthesis (BBN) around one second after the Big Bang. The one-second evolution of the Universe between inflation and BBN consists of a temperature decrease from $\sim 10^{16}$ GeV to several MeV, and yet science has uncovered almost nothing concrete about what occurs during this drastic temperature scale change.

The most basic models of inflation consist of one driving scalar field, the inflaton. Slow-roll inflation ends when the inflaton reaches the bottom of its potential well and begins to oscillate, eventually decaying. An oscillating scalar field at the bottom of a quadratic potential well, such as in "chaotic" inflation, follows the same dynamics as a pressureless fluid, namely what we call matter [2]. Therefore, a generic prediction of inflation is a brief period of domination by a matter-like energy source between the end of inflation and the onset of radiation domination at reheating. Other high-energy theories, such as string and M-theory, predict that after the inflaton decays, other oscillating scalar fields may briefly dominate the cosmic energy density in an early matter-dominated era (EMDE) [3]. In string theory, scalar fields called stabilized moduli are generic and important ingredients to realistic models whose energy density could dominate briefly after inflation [4]. Yet another possibility is that the inflaton or some other field decays into quasi-stable massive particles before BBN. The notion of a pre-BBN EMDE is a fairly general prediction of early universe

theories. With several potential theories predicting an EMDE, it is possible that there may be more than one EMDE before reheating. Of particular interest to the study of structure formation and evolution is the final EMDE that leads up to the point of reheating. This EMDE is particularly important because it generates the current content of the Universe. Reheating is often assumed to occur at extremely high temperatures ($\sim 10^{16}$ GeV), too early in the Universe's history to have much impact on observables. However, string theory predicts that the lightest stabilized moduli should have mass on order $\sim$1000 TeV, resulting in a reheat temperature less than a few hundred GeV [3]. This temperature scale is fairly general to other EMDEs predicted by string theory.

In an EMDE, the domination of this matter-like energy source, in the form of a scalar field, would enhance all matter density perturbation modes on scales up to the comoving Hubble horizon $R_H \equiv 1/[aH(a)]$, which is analagous to all wavenumbers $k > k_{\rm RH} = R_{\rm RH}^{-1}$. Here, $k_{\rm RH} = a_{\rm RH} H_{\rm RH}(a_{\rm RH})$ is the mode that enters the horizon at reheating [5]. At the end of the EMDE, the scalar field decays and radiation domination begins at the reheat temperature $T_{\rm RH}$, which is currently only constrained by BBN to be above 3 MeV [6, 7]. For low, GeV-scale reheat temperatures, the enhanced density perturbations will significantly increase the formation of dark matter microhalo populations at higher formation redshifts from that of a Universe that transitions directly from reheating to radiation domination. These microhalos predominantly lie within the sub-Earth mass regime, with higher densities due to earlier formation times compared to their counterparts that form in a standard radiation-dominated universe [8–10]. The increased formation of higher density substructure boosts the dark matter annihilation rate compared to the evolution without an EMDE because annihilation scales with the square of the dark matter density. Analytical calculations of this boost factor are on the order of $\sim 10^5$ [11]. These calculations are highly uncertain due to a lack of experimental data on interactions between microhalos and the effects on microhalo density profiles as a result of these interactions. In particular, it is unclear what the fate of the earliest forming microhalos will be. Ref. [11] concludes that N-body simulations of microhalos are necessary to determine if they can survive their absorption into larger microhalos that form slightly later. If the majority of the primordial microhalos do indeed survive, the boost factor will also be sensitive to how much of their mass is tidally stripped by their host halo.

In this work, we will attempt to determine this boost factor using cosmological N-body simulations and compare with prior analytical results. A more accurate boost factor will be necessary to determine if there is a viable parameter space of reheat temperatures, kinetic decoupling temperatures, and dark matter masses such that the EMDE produces results that agree with observations of the dark matter relic abundance. The dark matter in the enhanced substructure was created entirely through

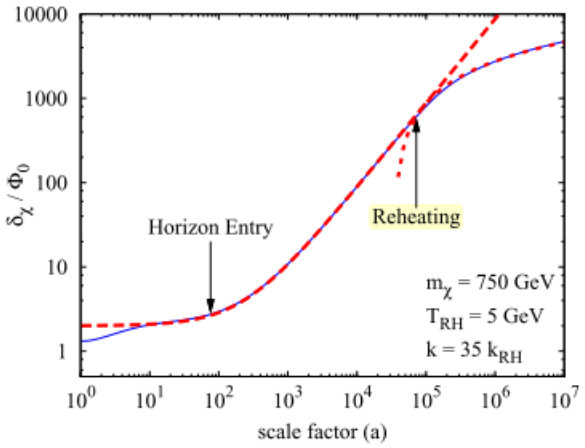

FIG. 1. Demonstration of linear enhancement due to an EMDE for subhorizon modes. Standard logarithmic growth begins at reheating. Figure from Ref. [11]

pair production, with no non-thermal dark matter generation due to scalar field decay. After dark matter freezes out, its comoving number density is conserved. However, during the EMDE, the matter-like scalar field acts as a source to the radiation, and thus additional photons are created. This causes the dark matter-radiation ratio to decrease. For the dark matter relic abundance to remain in agreement with current observational bounds from the *Planck* mission [12], freeze-out must occur earlier, and thus the annihilation cross section $\langle \sigma v \rangle$ must decrease from the standard value of 3×10^{-26} cm^3 s^{-1}. For observations to constrain an EMDE, the boost factor must be sufficiently large to compensate for a lower annihilation cross section in order to bring the dark matter annihilation rate above the current observable threshold.

The effects from an EMDE on the matter power spectrum will primarily depend on $T_{\rm RH}$ and the cut-off scale $k_{\rm cut}$ due to dark matter free-streaming. Causally connected density perturbation modes grow linearly with the scale factor during the EMDE. When the universe drops below the reheat temperature, the EMDE ends and radiation domination begins, and evolution of all subhorizon perturbation modes becomes logarithmic until matter-radiation equality. Scales that are larger than the cosmic horizon at reheating ($k < k_{\rm RH}$) will have experienced no density perturbation enhancement, only growing logarithmically since horizon entry. Figure 1 demonstrates this behavior for a mode that enters the horizon during an EMDE. Lower reheat temperatures result in a longer EMDE, which allows the density perturbations to grow larger.

After dark matter kinetically decouples from radiation at $T_{\rm kd}$, the remaining velocities of the dark matter particles create a free-streaming effect that reduces perturbations on scales below the free-streaming distance, which is the distance a DM particle has traveled since decoupling. This residual velocity determines the free-streaming cut-off scale, $k_{\rm cut}$, such that modes with $k > k_{\rm cut}$ are sup-

pressed due to free-streaming. Ultimately, the modes within the range $k_{\rm RH} < k < k_{\rm cut}$ will be enhanced by the EMDE. We first aim to establish the relationship between $k_{\rm RH}$ and $k_{\rm cut}$ as a function of the dark matter mass and the temperatures at reheating and kinetic decoupling.

The post-EMDE matter power spectrum can be used to run cosmological N-body simulations. Given a specific reheat temperature and free-streaming cut-off scale, a power spectrum can be generated and used as input for `GADGET-2` [13], a robust cosmological N-body simulator code. This simulates dark matter structure formation on small scales within a cube with side on the order of tens of parsecs/h, running through the cosmic dark ages up until a redshift of $z_f \sim 30$, allowing us to analyze increased microhalo populations as a result of the EMDE. Analytical models of an EMDE have shown an increase in the fraction of dark matter bound in microhalos from the standard $\sim 10^{-10}$ up to 50% for low reheat temperatures. We will use the results of these numerical simulations to verify theoretical results and analyze the structure of individual microhalos.

The focus of this thesis is to determine what happens to these microhalos as the universe evolves. As small microhalos merge with larger microhalos, they may remain intact as discrete subhalos within the larger host halo. It is also possible that the substructure is destroyed due to these mergers. Microhalo substructure drastically boosts the DM annihilation rate, which is quantified by the boost factor defined as:

$$1 + B_s = \frac{J}{\int \overline{\rho}_\chi^2 4\pi r^2 dr} \tag{1}$$

where J is the integral of density squared over the microhalo volume and the denominator is the integral over a halo with the same mass and virial radius but a smooth density profile. More substructure will cause J to increase, in turn increasing the boost factor. If enough substructure has survived in halos, the dark matter annihilation rate could be sufficiently boosted for detection using gamma ray telescopes. Of particular interest is the relative boost factor $(1 + B)/(1 + B_{\rm std})$, where $1 + B_{\rm std}$ is the standard substructure boost in annihilation due to subhalos above the reheat scale that form in the absence of an EMDE. Ref. [11] finds that if 90% of the dark matter is still contained in microhalos at $z = 50$, the relative boost from an EMDE is 100, which is not high enough to overcome the suppression in the annihilation cross section. However, if the microhalos form sufficiently early at $z = 400$ with 60% of dark matter bound into microhalos at that time, and these microhalos survive to today as subhalos within a larger host halo, the relative boost factor could be as large as 30,000. This boost factor would be sufficiently high to increase the dark matter annihilation rate in dwarf spheroidal galaxies above the observational limits of the *Fermi Gamma-Ray Telescope* [14].

The structure of this document is as follows: In Section II, we use numerical solutions to a system of coupled ordinary differential equations [15] to study the evolution of the phase space density of dark matter perturbation modes. We will study the perturbation dependence on $T_{\rm RH}$, $T_{\rm kd}$, and dark matter mass m_χ. Our ultimate goal in this section is to construct and verify an analytical model for the free-streaming cut-off scale as a function of the aforementioned temperatures and dark matter mass. We will attempt to determine a set of suitable parameters that result in a cut-off scale small enough to produce sufficient boost in annihilation. Once the relationship $k_{\rm cut}/k_{\rm RH}$ has been determined, we can generate the matter power spectrum and run cosmological simulations, which will be the focus of Section III. We will also employ the `Rockstar` [16] halo cataloging program to find the phase-space coordinates, masses, and radii of all well-resolved, gravitationally-bound structures in the simulation particle data. We will use these halo catalogs to compare the numerical halo mass functions to the analytical Sheth-Tormen [17] and Press-Schecter [18] mass functions. For further verification of the simulations, we will fit generalized Navarro-Frenk-White density profiles [19] to simulated halos and compare to analytical predictions for microhalos formed at high redshift. We will also discuss the mass-concentration relationship for microhalos. We will measure the evolution of the bound matter fraction of entire simulations as well as the substructure mass percentage of individual host halos. In Section IV, we will calculate the boost factor for microhalos and generate a boost-mass relationship $B_s(M_{\rm mh})$. This relationship will be integrated over all mass scales below the reheat mass to determine the total substructure boost for galaxy-mass host halos. These total boosts will be compared to observational limits for a given dark matter annihilation cross-section.

Note: Natural units ($\hbar = c = k_B = 1$) are used throughout this work.

II. FREE-STREAMING CUT-OFF SCALE

The linear enhancement from an EMDE is only present in modes that enter the horizon before reheating ($k > k_{\rm RH}$) and modes that are larger than the free-streaming cut-off scale ($k < k_{\rm cut}$). We seek to understand the dependence of the cut-off scale on the dark matter mass m_χ and the temperatures at reheating ($T_{\rm RH}$) and at kinetic decoupling ($T_{\rm kd}$).

Before kinetic decoupling, the dark matter is coupled to the lepton-photon plasma. After the Universe drops below $T_{\rm kd}$, the dark matter particles can be modeled as a collisionless gas. After reducing the Boltzmann equation for dark matter-lepton interactions to a Fokker-Planck equation for the evolution of dark matter density perturbations, Ref. [15] derives a system of coupled ordinary differential equations (Eq. (12)) to describe the evolution of the phase space density of each perturbation mode k.

We will now build up some of the necessary background in order to study this set of equations, introducing them

in Subsec. II C. In particular, we begin by introducing KDEMDE, the code used to study the evolution of the dark matter perturbations, in Subsec. II A. Then, we study the evolution of matter, radiation, and scalar field densities in Subsec. II B. In Subsec. II D, we will focus particularly on numerical effects due to the truncation of an infinite sum that is present due to the boxed terms in Eq. (12). Once we have generated data for the individual perturbation modes, we will study their relative magnitudes with the "transfer function" in Subsec. II E. Lastly, we will construct an analytical model of $k_{\rm cut}/k_{\rm RH}$ in Subsec. II F.

A. KDEMDE Introduction and Parameterization

The code to study Eq. (12), KDEMDE, was written by Cosmin Ilie in 2016. The following introduction to numerical evolution of perturbation modes is based on a document written by Cosmin Ilie. The parameters that describe the system are the reheat temperature $T_{\rm RH}$, the kinetic decoupling temperature in a standard radiation-dominated (RD) universe $T_{\rm kdS}$, the dark matter particle speed $c_\chi \equiv \sqrt{2T_{\rm kdS}/m_\chi}$, and the mode of interest relative to the mode that enters at reheating $k/k_{\rm RH}$. Note that the dark matter mass is fixed by the particle speed. The standard kinetic decoupling temperature is reached when the momentum transfer rate γ falls below the Hubble rate in a standard, radiation-dominated universe $H_{\rm RD}$, and is thus defined by $H_{\rm RD}(T_{\rm kdS}) = \gamma(T_{\rm kdS})$. Also, by focusing on the ratio $k/k_{\rm RH}$, we know that if $k/k_{\rm RH} > 1$, the mode enters the horizon before reheating, and if $k/k_{\rm RH} < 1$, the mode enters the horizon after reheating.

The mode that enters the horizon at a particular time is $k = R_H^{-1} = aH(a)$, where R_H is the comoving Hubble radius, as mentioned in the introduction. The mode that enters the horizon at reheating $k_{\rm RH} = a_{\rm RH}H(a_{\rm RH})$, where the Hubble parameter $H \propto a^{-3/2}$ during the EMDE. This is because during the EMDE, the dominant energy source is a pressureless fluid, namely the scalar field, whose energy density $\rho_\phi \propto a^{-3}$ and $H \propto \sqrt{\rho_\phi}$. This allows us to set the mode that enters the horizon at reheating as $k_{\rm RH} \equiv H_1\left(\frac{a_{\rm RH}}{a_I}\right)^{-3/2} a_{\rm RH}$, with H_1 being the Hubble parameter at a_I, the scale factor at the beginning of the code evolution.

As mentioned above, $T_{\rm kdS}$, the kinetic decoupling temperature in a standard RD background, is defined by:

$$\gamma(T_{\rm kdS}) = H_{\rm RD}(T_{\rm kdS}) = \sqrt{\frac{8\pi^3}{90 m_{\rm PL}^2} g_*(T_{\rm kdS}) T_{\rm kdS}^4} \tag{2}$$

with $m_{\rm PL} = \sqrt{1/G}$ the Planck mass and γ being the elastic scattering momentum transfer rate between leptons and the dark matter. The dark matter remains kinetically coupled to the radiation while $\gamma > H$. The momentum transfer rate scales as T_L^{4+n}, with T_L the lepton temperature and $n = 2$ in the case of p-wave scattering. By choosing $T_{\rm kdS}$, we can then compute the momentum transfer rate as a function of temperature:

$$\gamma(T) = \gamma(T_{\rm kdS})\left(\frac{T_L}{T_{\rm kdS}}\right)^6 \tag{3}$$

When the radiation is at a particular temperature during the EMDE, the additional contribution to the total energy density from the scalar field increases the expansion rate, since $H \propto \sqrt{\rho}$. When compared to a radiation-dominated Universe at the same temperature, the expansion rate of the Universe in an EMDE is faster, $H > H_{\rm RD}$. Therefore, if a standard, radiation-dominated Universe exhibits dark matter-radiation kinetic decoupling at $T_{\rm kdS}$ such that $H_{\rm RD}(T_{\rm kdS}) = \gamma(T_{\rm kdS})$, then for the Universe in an EMDE, $H(T_{\rm kdS}) > \gamma(T_{\rm kdS})$. Therefore, the dark matter must kinetically decouple at a higher temperature in an EMDE compared to the standard, radiation-dominated case. Ref. [20] finds that the kinetic decoupling temperature in an EMDE is $T_{\rm kd} \approx T_{\rm kdS}^2/T_{\rm RH}$ for $T_{\rm kdS} > T_{\rm RH}$. We are particularly interested in the case where the dark matter decouples from the plasma during the EMDE such that the two are not coupled at reheating, with $T_{\rm kdS} > T_{\rm RH}$. The radiation perturbations exhibit damped oscillations once the Universe becomes radiation-dominated, and this would also suppress the dark matter perturbations if the two remained kinetically coupled after reheating. In the case of $T_{\rm kdS} > T_{\rm RH}$, the kinetic decoupling temperature is defined as the solution to $\gamma(T_{\rm kd}) = H(T_{\rm kd})$. In Subsec. II F, we will discuss the implications of an intermediate state between the totally decoupled and fully coupled state termed "quasi-decoupling" [21] and its implications for calculating $k_{\rm cut}/k_{\rm RH}$. The remainder of our parameters are expressed in terms of $k/k_{\rm RH}$, $T_{\rm RH}$ and $T_{\rm kdS}$.

B. Background Evolution

The KDEMDE code uses a three-fluid model for reheating [5]:

$$\frac{d\rho_\phi}{dt} + 3H\rho_\phi = -\Gamma_\phi \rho_\phi \tag{4}$$

$$\frac{d\rho_r}{dt} + 4H\rho_r = \Gamma_\phi \rho_\phi \tag{5}$$

$$\frac{d\rho_\chi}{dt} + 3H\rho_\chi = 0 \tag{6}$$

Here, ϕ denotes the scalar field, r denotes radiation, and χ denotes the dark matter. The rate of radiation production is governed by Γ_ϕ, the rate of energy transfer from the scalar field to radiation. While solving this three-fluid system in Eqs. (4)-(6), the initial time t_I is chosen so that $a(t_I) \equiv a_I = 1$ and $H_1 \equiv H(a_I)$. The

scale factor a is the integration parameter, and we move forward with the following dimensionless quantities: $\tilde{\rho}_i = \rho_i/\rho_{\rm crit,1}$, for $i \in \{\phi, r, \chi\}$ and $\rho_{\rm crit,1} \equiv 3m_{\rm PL}^2 H_1^2/(8\pi)$ is the critical energy density at a_I. In order to reduce numerical instability, the a scaling is absorbed into each of the energy densities so that the quantities become: $\bar{\rho}_\phi \equiv \tilde{\rho}_\phi a^3$, $\bar{\rho}_r \equiv \tilde{\rho}_r a^4$, and $\bar{\rho}_\chi \equiv \tilde{\rho}_\chi a^3$. We can then rewrite Eqs. (4)-(6) as:

$$\frac{d\bar{\rho}_\phi}{da} + \frac{\Gamma_\phi}{H(a)a}\bar{\rho}_\phi = 0 \tag{7}$$

$$\frac{d\bar{\rho}_r}{da} - \frac{\Gamma_\phi}{H(a)}\bar{\rho}_\phi = 0 \tag{8}$$

$$\frac{d\bar{\rho}_\chi}{da} = 0 \tag{9}$$

The dark matter temperature, T_χ, obeys the following differential equation:

$$a\frac{dT_\chi}{da} + 2T_\chi = -2\Upsilon(a)(T_\chi - T_L) \tag{10}$$

with $\Upsilon(a) \equiv \gamma(T(a))/H(a)$, and γ defined in Eq. (3). The lepton temperature can be found by solving $\rho_r = \frac{\pi^2}{30} g_*(T_L) T_L^4$. We absorb the scaling for the dark matter temperature with $\bar{T}_\chi \equiv T_\chi a^2$. Thus, Eq. (10) becomes:

$$\bar{T}_\chi' = -2a\Upsilon(a)(\bar{T}_\chi a^{-2} - T_L) \tag{11}$$

C. Perturbation Evolution

With the background ODEs in place, we now introduce the system of coupled ODEs from Ref. [15] necessary to study the evolution of the phase space density f of each perturbation mode k:

$$\begin{aligned}
&\frac{df_{nl}}{da} + (2n+l)\left[\frac{\Upsilon(a)}{a} + \frac{R(a)}{H(a)a^2}\right] f_{nl} - 2n\frac{R(a)}{H(a)a^2} f_{n-1,l} \\
&+ \frac{kc_\chi}{H(a)a^2}\sqrt{\frac{T_L}{T_{\rm kdS}}}\Bigg\{\left(\frac{l+1}{2l+1}\right) \times \big[(n+l+\tfrac{3}{2}) \\
&\times \boxed{f_{n,l+1} - n f_{n-1,l+1}}\big] + \tfrac{l}{2l+1}\big(\boxed{f_{n+1,l-1}} - f_{n,l-1}\big)\Bigg\} \\
&= \delta_{l0}\big[-3\frac{d\Phi}{da}A_n - 2(-\frac{d\Phi}{da} + \frac{\Upsilon}{a}\mathcal{F}_*(\widetilde{\rho}_r)\frac{\delta_r}{4}\frac{T_L}{T_\chi})B_n\big] \\
&+ \delta_{l1}\frac{2k}{3H(a)a^2c_\chi}\sqrt{\frac{T_{\rm kdS}}{T_L}}(-\Phi + \Upsilon\frac{H(a)a}{k^2}\theta_r)A_n
\end{aligned} \tag{12}$$

where Φ represents the gravitational potential, θ_r is the radiation perturbation velocity, and both δ_{l0} and δ_{l1} are Kronecker delta functions. The radiation and scalar field perturbations follow ODEs that are omitted in this manuscript, but can be found in the appendix of Ref. [5]. To study the dark matter perturbations, we can now employ Eq. (12), noting that we have already made the necessary changes of variables in accordance with our scaling-absorbed terms. In Eq. (12), we use several additional functions, defined as follows:

$$\begin{aligned}
R(a) &\equiv \frac{d}{d\tau}\ln(aT_L^{1/2}), \\
A_n(a) &\equiv \Big(1 - \frac{T_\chi}{T_L}\Big)^n, \\
B_n(a) &\equiv n\Big(\frac{T_\chi}{T_L}\Big)\Big(1 - \frac{T_\chi}{T_L}\Big)^{n-1}, \\
\mathcal{F}_*(\tilde{\rho}_R) &\equiv \Big(1 + \frac{1}{4}\frac{d\ln g_*}{d\ln T_L}\Big)^{-1}.
\end{aligned} \tag{13}$$

We can eliminate τ by rewriting $R(a)$ as:

$$R(a) = H(a)a\left[1 + \frac{1}{2T_L}\frac{dT_L}{d\tilde{\rho}_r}\left(-4\tilde{\rho}_r + \frac{\Gamma_\phi}{H(a)}\tilde{\rho}_\phi\right)\right] \tag{14}$$

Lastly, we can use $\frac{dT_L}{d\tilde{\rho}_r} = \frac{1}{4}\frac{T_L}{\tilde{\rho}_r}\mathcal{F}_*(\tilde{\rho}_r)$ to get:

$$\frac{R}{H(a)a^2} = \frac{1}{a}\left[1 + \mathcal{F}_*(\tilde{\rho}_r)\left(\frac{\Gamma_\phi}{8H(a)}\frac{\tilde{\rho}_\phi}{\tilde{\rho}_r} - \frac{1}{2}\right)\right] \tag{15}$$

As previously mentioned, f_{nl} is the dark matter phase space density, with the density perturbation $\delta_\chi = f_{00}$. While we are only interested in $\delta_\chi = f_{00}$, the evolution of this density depends on infinite expansions in n and l. The expansion in n is a result of the decomposition of the momentum dependence of the dark matter phase space density into eigenfunctions of the Fokker-Planck operator. These eigenfunctions contain a generalized Laguerre polynomial with index n. The expansion in l is a result of a spherical harmonic in the expanded eigenfunctions. Typically a spherical harmonic includes a second index m, but due to the rotational symmetry of dark matter-lepton scattering, we are only concerned with the $m = 0$ term in the spherical harmonic expansion.

We now have a full model of dark matter perturbation evolution that we can explore via numerical calculations. In the simulation code, we will primarily operate under the condition of constant g_*, which is the parameter of relativistic degrees of freedom that changes with the plasma temperature.

Two separate versions of KDEMDE are employed in order to separately address the two cases of $k/k_{\rm RH} > 1$ and $k/k_{\rm RH} < 1$. In both versions, the initial scale factor is set to $a_I = 1$. For $k/k_{\rm RH} > 1$, horizon entry is fixed at $a_{\rm HOR} = 100$, and reheating occurs at $a_{\rm RH} = a_{\rm HOR}(k/k_{\rm RH})^2$. Since this version handles only $k/k_{\rm RH} > 1$, namely the modes that enter the horizon before reheating, we have guaranteed that $a_{\rm RH} > a_{\rm HOR}$. Lastly, we set the final scale factor of evolution $a_f = n_f a_{\rm RH}$, with n_f varying from 100 to 1000, such that

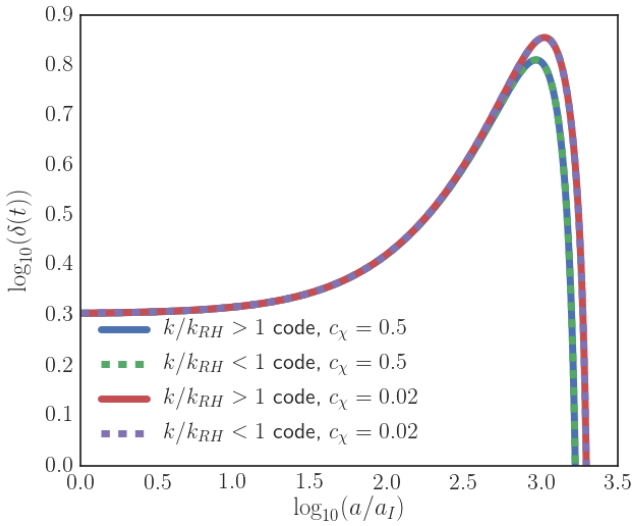

FIG. 2. Comparison between two versions of EMDE code for $k/k_{\rm RH} \approx 1$, where both versions should function properly. At higher c_χ, free-streaming suppression becomes noticeable at late times. The rapid decay is due to radiation coupling, as this test case is for $T_{\rm RH} > T_{\rm kdS}$, and $\delta_r \to 0$ at reheating [5].

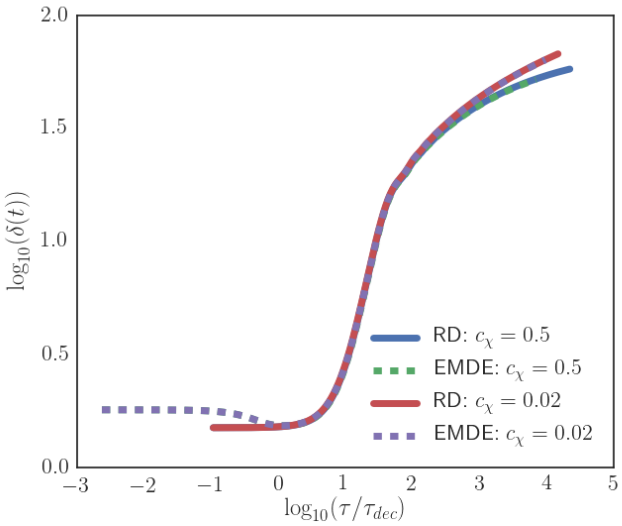

FIG. 3. For a mode that enters the horizon after the EMDE has ended with $k/k_{\rm RH} \approx 0.001$, the perturbation evolution from a code that assumes strict radiation-domination agrees with KDEMDE. Notice the free-streaming suppression at higher values of c_χ.

the mode can evolve sufficiently long for us to observe free-streaming effects and study the time evolution of the modes.

In this case of $k/k_{\rm RH} < 1$, the user selects the $a_{\rm RH}$ value. The scale factor at horizon entry $a_{\rm HOR}$ can then be found by solving $k = a_{\rm HOR}H(a_{\rm HOR})$. It is important to note that these modes enter the horizon after reheating, namely $a_{\rm HOR} > a_{\rm RH}$. This code also evolves the perturbation until $a_{fin} = n_f a_{\rm RH}$. As a consistency check, we verify that the results of the two versions of the code agree in the limit of $k/k_{\rm RH} \approx 1$. We evolve a mode out to low $a_f = 100 a_{\rm RH}$, with the density evolutions seen in Figure 2.

A third version of the code was written that evolves perturbation modes in the absence of an EMDE, assuming only radiation domination. We use this version of the code to verify the functionality of KDEMDE for the case of a mode with $k/k_{\rm RH} < 1$. This mode should be unaffected by the EMDE since reheating occurs before this mode enters the horizon. Figure 3 demonstrates that KDEMDE does indeed correctly model the evolution of a perturbation mode in the absence of an EMDE. With these consistency checks in place, we can begin testing the evolution limits of KDEMDE.

D. Truncation Analysis

The system of ODEs that govern the evolution of the perturbed dark matter phase-space density is infinite and thus must be truncated in order to numerically solve for f_{00}. Since we cannot numerically evolve an infinite number of ODEs, we must choose some $N_{\rm max}$ and $L_{\rm max}$ above which we truncate the expansions in n and l. As seen in the boxed terms in Eq. (12), truncation error will initially be present in the $f_{N_{\rm max},l}$ and $f_{n,L_{\rm max}}$ terms for all $n \leq N_{\rm max}$ and $l \leq L_{\rm max}$. As the perturbation modes evolve, this error will make its way down the n, l ladders until it begins to dominate in the f_{00} mode. This means that the truncation error can prohibit accurate perturbation evolution to high a_f. The first boxed term in Eq. (12) is proportional to kc_χ, so we will not be able to successfully evolve out to as high of an a_f for larger c_χ and k.

In order to generate a matter power spectrum at $z_i = 2000$ for our EMDE simulations, we will need to know the ratio $k_{\rm cut}/k_{\rm RH}$ evaluated today. Since `GADGET-2` does not have the capability of simulating the random thermal motions of individual dark matter particles in order to evolve the free-streaming cut-off scale, the input power spectrum for the simulations must use the value of $k_{\rm cut}/k_{\rm RH}$ evaluated today, rather than evaluated at the redshift where the simulation begins.

However, in order to calculate $k_{\rm cut}/k_{\rm RH}$ today, we find that the evolution from matter-radiation equality to today is trivial. We primarily focus on evaluating $k_{\rm cut}/k_{\rm RH}$ up to matter-radiation equality, adding in the evolution up until today at the end. All of our numerical data from KDEMDE is in the time period between reheating and matter-radiation equality, so the subsequent model design and fitting focuses on correctly matching the behavior in that time period. To find the scale factor at matter-radiation equality $a_{\rm eq}$ as a function of the reheat temperature, we employ the "conservation of entropy"

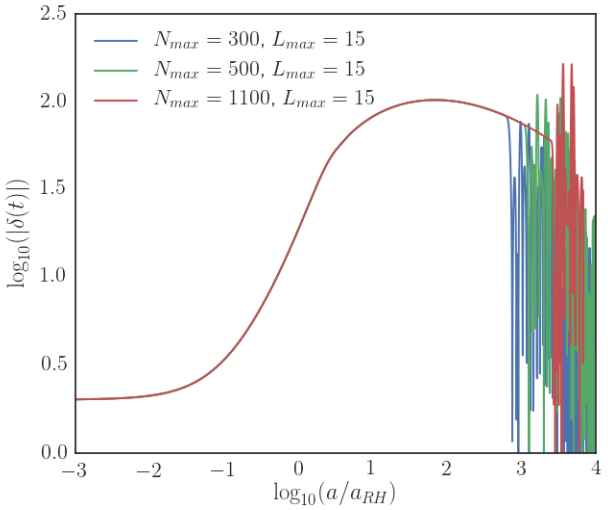

FIG. 4. Example of truncation error in the perturbation mode for several values of $N_{\max}$. The code begins to break down at $a \approx 10^3 a_{\rm RH}$ in this case, but for high $k/k_{\rm RH}$ the error dominates much earlier.

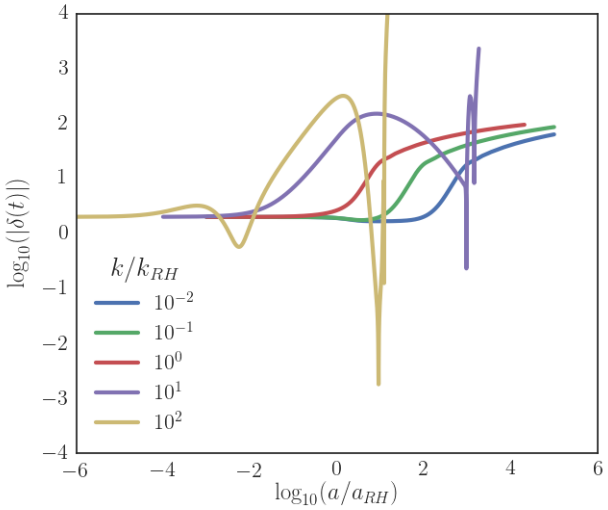

FIG. 5. Evolution and breakdown of various values of $k/k_{\rm RH}$ at high $c_\chi = 0.5$. For the modes with $k/k_{\rm RH} \geq 1$, the initial increase in $\delta(t)$ occurs due to horizon entry. Note the logarithmic growth after horizon entry as expected.

equation from cosmology:

$$g_{*,eq} a_{\rm eq}^3 T_{\rm eq}^3 = g_{*,\rm RH} a_{\rm RH}^3 T_{\rm RH}^3 \tag{16}$$

In much of our analysis of the perturbation evolutions, we will focus our interests on $T_{\rm RH} = 5$ GeV. The temperature at $a_{\rm eq}$ was approximately 0.75 eV. Lastly, the g_* factor at $a_{\rm eq}$ is 3.91 and at a reheating temperature of 5 GeV, $g_* = 85.6$. Thus we expect that in terms of the reheat scale factor set by the code,

$$a_{\rm eq} = 1.9 \times 10^{10} a_{\rm RH}. \tag{17}$$

Unfortunately, this is substantially further out than the code is able to successfully evolve a perturbation mode. By studying the results of KDEMDE for various configurations of $T_{\rm RH}$, $T_{\rm kdS}$, and c_χ out to a_f between 100 and 1000, we will be able to construct an analytical model of $k_{\rm cut}/k_{\rm RH}$ that agrees with the numerics and predicts out to a_0. This discussion will be the focus of Subsection II F.

We are interested in determining the $N_{\max}$ and $L_{\max}$ that is necessary to evolve a mode $k/k_{\rm RH}$ out to a particular a_f. We expect that these values of $N_{\max}$ and $L_{\max}$ will be sensitive to the particular truncation scheme employed. As a first pass, we define our truncated terms such that:

1. Set both $f_{n,l+1} = 0$ and $f_{n-1,l+1} = 0$ when $l = L_{\max}$
2. Set $f_{n+1,l-1} = 0$ when $n = N_{\max}$

The effects of truncation can be seen quite clearly in Figure 4. For a perturbation mode that enters only briefly before reheating ($k/k_{\rm RH} = 5$) with a moderately high particle speed ($c_\chi = 0.5$), we see that the truncation error begins to dominate the f_{00} term at around $10^3 a_{\rm RH}$, which allows the mode to evolve sufficiently long for our necessary analysis. Unfortunately, for higher $k/k_{\rm RH}$, it becomes much more difficult to reach $10^3 a_{\rm RH}$ successfully. By increasing $N_{\max}$, we are capable of pushing out to further values of a_f before the error begins to dominate. Unfortunately, as $N_{\max}$ is increased, we begin to see diminishing returns in successful a_f. The point where continuing to increase $N_{\max}$ becomes computationally intractable for analysis of a large parameter space in temperature, c_χ, and $k/k_{\rm RH}$ is around $N_{\max} \approx 2000$. We note that the code requires a much lower value of $L_{\max}$, on the order of 10. For low values of $k/k_{\rm RH}$, increasing $L_{\max}$ past approximately 15 provides no increase in successful a_f. This dependence on $N_{\max}$ and $L_{\max}$ seems to reverse at high $k/k_{\rm RH}$, which will be discussed below.

As mentioned above, the truncation terms in Eq. (12) are proportional to kc_χ. Because of this, we expect that the truncation error will begin to dominate earlier at higher $k/k_{\rm RH}$. To confirm this expectation, we plot the perturbation evolution for several orders of magnitude of $k/k_{\rm RH}$ in Figure 5. Since the truncation error should increase with c_χ as well, we deliberately use a high $c_\chi = 0.5$ so that we study the worst-case scenario, namely the lowest possible a_f out to which the code can successfully evolve for a given $k/k_{\rm RH}$. For $k/k_{\rm RH} = 10^2$, we see that the truncation error begins to dominate at an unfortunately low $a_f \approx 10 a_{\rm RH}$. In order to study $k_{\rm cut}/k_{\rm RH}$, we will need the code to successfully evolve out to approximately $a_f = 1000 a_{\rm RH}$ and up to $k/k_{\rm RH} \approx 100$. Thankfully, for the majority of the parameter space that we are interested in, c_χ is substantially less than 0.5.

As noted above, the perturbation evolution is signifi-

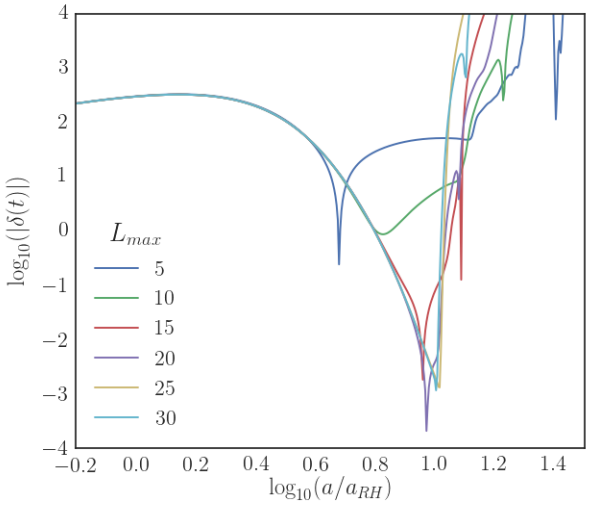

FIG. 6. At high values of $k/k_{\rm RH}$, increasing $L_{\rm max}$ results in successful evolution out to higher a_f. Here, we are using $N_{\rm max} = 1500$. We test high $c_\chi = 0.5$ to probe the upper extreme of speeds that we will eventually study.

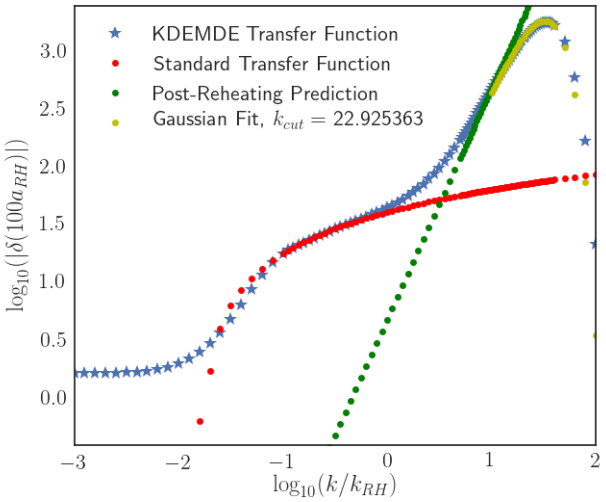

FIG. 7. Transfer function at $100a_{\rm RH}$ for $c_\chi = 0.1$, and $T_{\rm kdS}/T_{\rm RH} = 2$. The standard transfer function corresponds to the expected evolution at $100a_{\rm RH}$ in the absence of an EMDE. The post-reheating prediction attempts to match the growth of modes which enter the horizon before the EMDE ends. The difference between this predicted slope and the one seen in the transfer function is likely due to plasma interactions while still coupled at $k/k_{\rm RH} > k_{\rm kd}/k_{\rm RH} \approx 30$. The Gaussian fit is found using Eq. (21).

cantly more sensitive to $N_{\rm max}$ for low $k/k_{\rm RH}$, which can be seen in Figure 4. However, for $\ln(k/k_{\rm RH}) \approx 1$ to 2, we find that increasing $L_{\rm max}$ affords an appreciable increase in successful evolution time for large $k/k_{\rm RH}$ modes. This can be seen in Figure 6, where going from $L_{\rm max} = 5$ to $L_{\rm max} = 30$ gains half an order of magnitude of successful evolution for a $k/k_{\rm RH} = 100$ mode.

Ultimately, we were unable to find truncation schemes that allow for successful evolution out to high a_f for arbitrarily high c_χ and $k/k_{\rm RH}$. However, our truncation tests were predominantly for the case of $c_\chi = 0.5$, and we will show below that we will generally be interested in lower values of c_χ. In our discussion of transfer functions, we find that even with the basic truncation schemes employed above, we manage to evolve the necessary modes out to a range of a_f between 100 and 1000. For high values of $k/k_{\rm RH}$ and c_χ, we simply increase the values of $N_{\rm max}$ and $L_{\rm max}$ until the mode can successfully evolve out to the a_f of interest.

E. Transfer Functions

We now introduce the notion of a transfer function. Fig. 5 shows the perturbation δ_χ as a function of scale factor for multiple $k/k_{\rm RH}$. Suppose that we choose a fixed time a_f and want to know the values of δ_χ for each $k/k_{\rm RH}$. This is the transfer function, defined as

$$T(k) = \frac{\delta_\chi(k)}{\delta_0}\Big|_{a_f}, \tag{18}$$

with δ_0 the initial perturbation amplitude at some fixed a_i. KDEMDE defines all initial perturbations to have $\delta_0 = 1$. We begin at $a_f = 100a_{\rm RH}$ and observe the transfer function for several orders of magnitude of $k/k_{\rm RH}$ in Fig. 7. The transfer function is calculated using KDEMDE by evolving many modes between $10^{-3} < k/k_{\rm RH} < 10^2$. The transfer function $T(k)$ relates the matter power spectrum $P(k)$ to the primordial power spectrum generated during inflation $\tilde{P}(k)$ by

$$P(k) = T(k)^2 \tilde{P}(k) \tag{19}$$

Fig. 7 demonstrates a significant boost due to the EMDE for $k > k_{\rm RH}$ and $k < k_{\rm cut}$. Here, $k_{\rm cut}$ approximately corresponds to the peak of the transfer function, although we will define it more rigorously below. Unfortunately, this power spectrum is only evaluated out to $a_f = 100a_{\rm RH}$, otherwise the large gap between $k_{\rm cut}$ and $k_{\rm RH}$ for a temperature ratio as low as $T_{\rm kdS}/T_{\rm RH} = 2$ would be quite compelling. However, our matter power spectrum is only concerned with $k_{\rm cut}/k_{\rm RH}$ at a_0. We expect that $k_{\rm cut}/k_{\rm RH}$ will decrease logarithmically with a, a result that will be confirmed in Subsec. II F with our analytic model.

The post-reheating amplitudes of modes that enter during the EMDE with $k > k_{\rm RH}$ are expected to agree with the following equation from Ref. [11]:

$$\delta_{\chi,PR}(k > k_{\rm RH}) = \frac{2}{3}\left(\frac{k/k_{\rm RH}}{0.86}\right)^2\left[1 + \ln\left(\frac{a/a_{\rm RH}}{1.29}\right)\right]. \tag{20}$$

This is the curve labeled "Post-Reheating Prediction" in Fig. 7. Interestingly, the slope of the curve in Eq. (20)

does not quite agree with the results of the numerical simulations, as seen in Fig. 7. The lower slope found in the numerical computations is due to interactions between the plasma and the dark matter that are not modeled in Eq. (20).

We now describe our technique for determining the $k_{\rm cut}$ value for a given transfer function. In the absence of free-streaming, the post-reheating transfer function for modes with $k > k_{\rm RH}$ obeys Eq. (20). However, due to free-streaming, modes above the free-streaming cut-off scale are suppressed. We multiply a Gaussian with Eq. (20) to model the peak of the transfer function, with the form:

$$\delta_{\chi,Gauss}(k > k_{\rm RH}) = \delta_{\chi,PR}(k) e^{-k^2/(2k_{\rm cut}^2)} \tag{21}$$

A demonstration of this fitting can be seen in Fig. 7. It is important to note that the value of $k_{\rm cut}$ determined by the fit is not the peak of the transfer function, but rather the optimal $k_{\rm cut}$ such that Eq. (21) best fits the numerical results from KDEMDE. In order to generate the fit, we use the `curve_fit` routine from the SciPy package for Python. We only use data for $k/k_{\rm RH} \geq 10$ for the fit.

After reheating, the Universe becomes radiation-dominated and δ_χ exhibits logarithmic growth after horizon entry for each mode. Ref. [22] provides an equation that describes the transfer function for a radiation-dominated Universe with no free-streaming:

$$\delta_{\chi,RD}(k) = \frac{10}{9}\Phi_0\left[A \ln\left(B\frac{a}{a_{\rm HOR}}\right)\right] \tag{22}$$

with $A = 9.11$, $B = 0.594$ and in KDEMDE, $\Phi_0 = 1.0$. For each mode, the scale factor at horizon entry $a_{\rm HOR}$ is defined as the solution to $k = a_{\rm HOR}H(a_{\rm HOR})$. This is the curve labeled "Standard Transfer Function" in Fig. 7.

The values of $m_\chi/T_{\rm RH}$ that provide the best opportunity for a detectable boost in the dark matter annihilation rate are in the range of $m_\chi/T_{\rm RH} \approx 100 - 200$ [11]. We need $m_\chi/T_{\rm RH} > 100$ such that the dark matter abundance freezes out during the EMDE, rather than exponentially declining until some later point during radiation domination. We would like $m_\chi/T_{\rm RH} < 200$ such that the annihilation cross section does not become so low as to push annihilation signatures well below the detection threshold for the foreseeable future. For a given $T_{\rm kdS}$ and $T_{\rm RH}$, we can determine the optimum c_χ value to probe this $m_\chi/T_{\rm RH}$ range by relating c_χ to this ratio as such:

$$m_\chi/T_{\rm RH} = \frac{1}{c_\chi^2}\frac{2T_{\rm kdS}}{T_{\rm RH}} \tag{23}$$

The majority of the work thus far has been done with the temperatures $T_{\rm kdS} = 10$ GeV and $T_{\rm RH} = 5$ GeV, and thus this optimal range of $m_\chi/T_{\rm RH}$ ratios corresponds to $c = 0.14$ to $c = 0.2$. For each temperature ratio, we will have to modulate the values of c_χ to fit the desirable $m_\chi/T_{\rm RH}$ accordingly. Figure 8 demonstrates that only the ratio of the temperatures affects the transfer function, and ultimately $k_{\rm cut}/k_{\rm RH}$, rather than the individual values of $T_{\rm RH}$ and $T_{\rm kdS}$. We will use transfer functions to explore $T_{\rm kdS}/T_{\rm RH}$ ratios between 2 and 6. Above this, KDEMDE struggles to successfully evolve to high enough a_f to generate transfer functions. We will construct our analytical model of $k_{\rm cut}/k_{\rm RH}$ and nail down its dependence on $T_{\rm kdS}/T_{\rm RH}$, c_χ, and a_f in Subsec. II F, comparing to all transfer function data available.

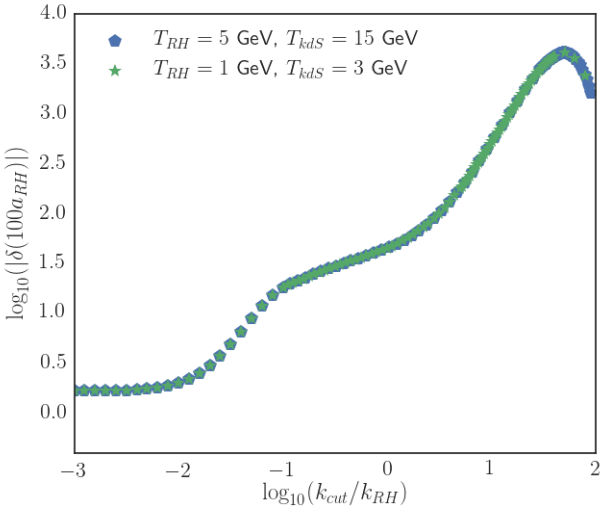

FIG. 8. Transfer function at $c_\chi = 0.18$ for two different sets of $T_{\rm RH}$ and $T_{\rm kdS}$, both of which have $T_{\rm kdS}/T_{\rm RH} = 3$. The transfer function is agnostic to the actual temperatures, only caring about the ratio.

F. Analytical Model of Free-Streaming Cut-off

We seek to build an analytical model that can accurately predict $k_{\rm cut}/k_{\rm RH}$ for general c_χ and $T_{\rm kdS}/T_{\rm RH}$. Here we provide a derivation of a general form for $\frac{k_{\rm cut}}{k_{\rm RH}}$. Afterward, we fit the model against our numerical results and discover a remarkable simplification. This simplified model is used to predict the $k_{\rm cut}/k_{\rm RH}$ at a_0. Ultimately, we will determine the minimum $T_{\rm kdS}/T_{\rm RH}$ that will provide sufficiently high $k_{\rm cut}/k_{\rm RH}$ to generate significant annihilation boosts.

At kinetic decoupling, the dark matter particles begin to free stream. The physical size of the free-streaming horizon $l_{fs} = \int v_\chi dt$. It is important not to confuse v_χ with c_χ. Here, v_χ is the true physical dark matter particle speed. Defined in terms of the comoving distance λ, we have that $l_{fs} = a\lambda$. We define the comoving free-streaming horizon $\lambda_{\rm fs}$ such that:

$$\lambda_{\rm fs} \equiv \int d\lambda = \int_{a_{\rm kd}}^{a_f} \frac{v_\chi dt}{a} = \int_{a_{\rm kd}}^{a_f} v_\chi \frac{da}{a^2 H} \tag{24}$$

We integrate from decoupling to a_f, where we choose a_f in terms of $a_{\rm RH}$. We will eventually be interested in $a_f = a_0$, namely the scale factor today. The last step in the equation above comes from the fact that $dt = \frac{da}{da/dt} = \frac{da}{Ha}$. The free-streaming horizon $\lambda_{\rm fs}$ corresponds to a fourth of the free-streaming cut-off wavelength $\lambda_{\rm cut}$. Therefore, the free-streaming cut-off wavenumber can be defined in terms of the horizon:

$$k_{\rm cut} = \frac{2\pi}{\lambda_{\rm cut}} = \frac{2\pi}{4\lambda_{\rm fs}} \approx \frac{1}{\lambda_{\rm fs}} \tag{25}$$

In our model, we begin by employing a piecewise functional form for $H(a)$ and $v_\chi(a)$. Using the relationship that $k_{\rm RH} = a_{\rm RH}H(a_{\rm RH}) = a_{\rm RH}H_{\rm RH}$, we have:

$$H(a) = \begin{cases} b_H H_{\rm RH}\left(\frac{a}{a_{\rm Ht}}\right)^{-3/2} & a \le a_{\rm Ht} \\ b_H H_{\rm RH}\left(\frac{a}{a_{\rm Ht}}\right)^{-2} & a > a_{\rm Ht} \end{cases} \tag{26}$$

with $a_{\rm Ht} = 1.0872 a_{\rm RH}$ corresponding to the Hubble transition point and $b_H = 0.882$ being a fit parameter. Here, $H \propto a^{-3/2}$ before the Hubble transition because the Universe is still in a phase of matter domination, whereas $H \propto a^{-2}$ after the transition because the Universe has transitioned to the radiation dominated era. We define the dark matter velocity using another piecewise form:

$$v_\chi(a) = \begin{cases} b_v\sqrt{\frac{T_{\rm kd}}{m_\chi}}\left(\frac{a_{\rm kd}}{a}\right)^{9/16} & a \le a_v \\ b_v\sqrt{\frac{T_{\rm kd}}{m_\chi}}\left(\frac{a_{\rm kd}}{a_v}\right)^{9/16}\left(\frac{a_v}{a}\right) & a > a_v. \end{cases} \tag{27}$$

The velocity $v_\chi \propto \sqrt{T_\chi}$, and Ref. [21] shows that before the dark matter fully decouples from the radiation, it is in a quasi-decoupled state where $T_\chi \propto a^{-9/8}$. The dark matter becomes fully decoupled at a_v, after which $T_\chi \propto a^{-2}$. Here, a_v and b_v are fit parameters yet to be determined. We initially demand that $a_v > a_{\rm Ht}$ which yields three separate pieces for our integral of $\lambda_{\rm fs}$, namely the cases where $a < a_{\rm Ht}$, $a_{\rm Ht} < a < a_v$, and $a > a_v$. Recalling that c_χ controls our value of m_χ, we can rewrite our equations for v_χ in terms of $c_\chi = \sqrt{2T_{\rm kdS}/m_\chi}$. We also need the relationship $T_{\rm kd} = r\frac{T_{\rm kdS}^2}{T_{\rm RH}}$ where for constant g_* as in KDEMDE we have that $r = \sqrt{5/2}$.

We will also need $a_{\rm kd}$, the scale factor at kinetic decoupling during the EMDE. This is found with:

$$\frac{a_{\rm RH}}{a_{\rm kd}} = \left(\frac{T_{\rm kd}}{T_{\rm RH}}\right)^{8/3}\left[\frac{2}{5}\frac{g_{*,\rm RH}}{g_{*,\rm kd}}\right]^{-2/3} \tag{28}$$

Once again, we employ constant g_*, and thus $g_{*,\rm RH} = g_{*,\rm kd}$. We can now express $a_{\rm kd}$, $T_{\rm kd}$, and m_χ in terms of our preferred parameters $T_{\rm kdS}$, $T_{\rm RH}$, and c_χ. The integral in Eq. (24) is thus split into the three piecewise terms and evaluated. We multiply a factor of $k_{\rm RH}$ onto both sides and find:

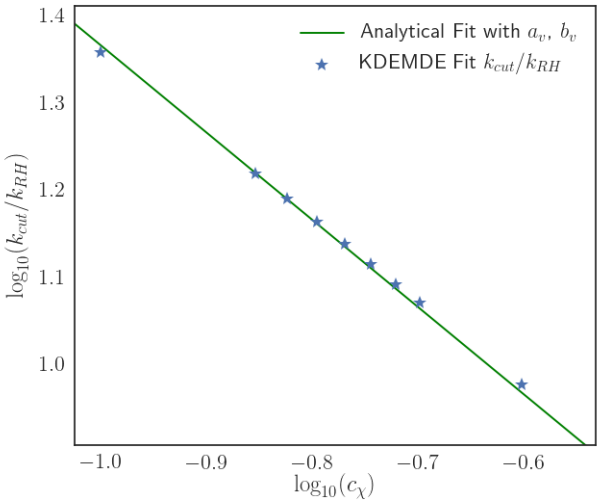

FIG. 9. Using temperatures $T_{\rm kdS} = 10$ GeV and $T_{\rm RH} = 5$ GeV at $a_{\rm f} = 100a_{\rm RH}$, this figure demonstrates the c_χ^{-1} dependence of $k_{\rm cut}/k_{\rm RH}$. The model from Eq. (29) is fit to the data points from transfer function fits of KDEMDE evolutions. The fit values were $a_v = 1.57a_{\rm RH}$ and $b_v = 0.64$.

$$\begin{aligned}\frac{k_{\rm RH}}{k_{\rm cut}} = k_{\rm RH}\lambda_{\rm fs} = \frac{b_v}{b_H}\frac{c_\chi}{\sqrt{2}r}\left(\frac{T_{\rm RH}}{T_{\rm kdS}}\right)^{5/2}\left(\frac{2}{5}\right)^{3/8}\left(\frac{a_{\rm RH}}{a_{\rm Ht}}\right)^{\frac{25}{16}} \\ \times\left[16\left(\left(\frac{a_{\rm Ht}}{a_{\rm kd}}\right)^{\frac{1}{16}}-1\right)+\frac{16}{7}\left(\left(\frac{a_v}{a_{\rm Ht}}\right)^{\frac{7}{16}}-1\right)\right. \\ \left.+\left(\frac{a_v}{a_{\rm Ht}}\right)^{\frac{7}{16}}\ln\left(\frac{a_f}{a_v}\right)\right]\end{aligned} \tag{29}$$

We now have all quantities in Eq. (29) defined except for a_v and b_v. Note that the quantity that we are interested in $k_{\rm cut}/k_{\rm RH}$ is simply the inverse of Eq. (29). This equation shows two important parameter dependences for $k_{\rm cut}/k_{\rm RH}$. Firstly, $k_{\rm cut}/k_{\rm RH} \propto c_\chi^{-1}$. As c_χ increases, $k_{\rm cut}$ should become smaller because the dark matter will be able to travel a greater distance in the age of the Universe. Therefore, larger spatial mode perturbations will be flattened out. This c_χ^{-1} dependence is confirmed with numerical transfer functions from KDEMDE. Secondly, $k_{\rm cut}/k_{\rm RH} \propto (T_{\rm kdS}/T_{\rm RH})^{5/2}$, so an increase in the temperature ratio will greatly increase $k_{\rm cut}/k_{\rm RH}$.

As a first-pass test of our model, we treat a_v and b_v as fit parameters. Holding $T_{\rm kdS}/T_{\rm RH}$ fixed, we plot the numerically-determined $k_{\rm cut}$ values from the KDEMDE transfer function fits as a function of c_χ in Fig. 9. Using these data points, we employ a curve-fitting routine to determine the optimum a_v and b_v that best predicts the $k_{\rm cut}/k_{\rm RH}$ for all c_χ values at a particular temperature ratio. As demonstrated in the figure, this method is fairly successful at $a_f = 100a_{\rm RH}$ for this particular temperature ratio $T_{\rm kdS}/T_{\rm RH} = 2$. However, when the values of

a_v and b_v from the initial fit are then used to predict the $k_{\rm cut}/k_{\rm RH}$ for $T_{\rm kdS}/T_{\rm RH} = 3$ to 5, the model does a poor job of reproducing the numerical results, being off by as much as 25% at $a_f = 100a_{\rm RH}$. Since we are trying to predict out to substantially further times, it is important to have fit parameters that provide a model that agrees to high precision with our numerical results at low a_f. For example, $a_v/a_{\rm RH} = 1.573$ as fit from the $T_{\rm kdS}/T_{\rm RH} = 2$ data, but $a_v/a_{\rm RH} = 1.223$ as fit from the $T_{\rm kdS}/T_{\rm RH} = 3$ data, introducing a serious discrepancy when attempting to predict $k_{\rm cut}/k_{\rm RH}$ for a specific temperature ratio when using fit parameters found from another temperature ratio's numerical results. The conclusion is that a_v and b_v must depend on temperature. Therefore, we seek to capture this temperature dependence in our model such that the fit parameter values are consistent across different temperature ratios.

In deriving a model for a_v and b_v, we utilize two key constraints. Since the temperature of the dark matter particle is $T_\chi \sim v_\chi^2 m_\chi$, we can use constraints on the dark matter temperature to determine v_χ up to a constant, and then solve for b_v. Ref. [23] provides an analytical model of the dark matter temperature:

$$T_\chi^A(s) = T_\gamma s^\lambda e^s \Gamma(1-\lambda, s) \tag{30}$$

with $s = \frac{2}{\alpha\beta}(\frac{a_{\rm kd}}{a})^{\alpha\beta}$, $\lambda = \frac{2-\alpha}{\alpha\beta}$, and $\alpha = 3/8$, $\beta = 4+n-\nu$. Here, $n = 2$ for p-wave scattering and $\nu = 4$ in an EMDE. $\Gamma(1-\lambda, s)$ is the incomplete Γ-function. The general form of Eq. (28) allows us to solve for the background radiation temperature T_γ:

$$\frac{T_\gamma}{T_{\rm RH}} = \left[\left(\frac{a}{a_{\rm RH}}\right)\left(\frac{5}{2}\right)^{2/3}\right]^{-3/8} \tag{31}$$

under the use of constant g_*. Since the dark matter temperature is $T_\chi \sim v_\chi^2 m_\chi$, we can write T_χ in terms of v_χ from Eq. (27):

$$T_\chi(a) = \begin{cases} b_v^2 T_{\rm kd}\left(\frac{a_{\rm kd}}{a}\right)^{9/8} & a \le a_v \\ b_v^2 T_{\rm kd}\left(\frac{a_{\rm kd}}{a_v}\right)^{9/8}\left(\frac{a_v}{a}\right)^2 & a > a_v \end{cases} \tag{32}$$

Numerical comparison between the analytical temperature and the true dark matter temperature show that, for $a \gg a_{\rm RH}$, the analytical model of the dark matter temperature T_χ^A should relate to the true dark matter temperature T_χ by:

$$\frac{T_\chi(a)(a/a_{\rm RH})^2}{T_\chi^A(a_{\rm RH})} \approx 1.37 \tag{33}$$

At early times, for $a < 0.1a_{\rm RH}$, the analytical temperature model is effectively exact, and thus we set $T_\chi(a) = T_\chi^A(a)$ for $a \le 0.1a_{\rm RH}$. We solve the model temperature from Eq. (32) at $a < a_v$ for b_v:

$$b_v = \sqrt{\frac{T_\chi(a)}{T_{\rm kd}}}\left(\frac{a}{a_{\rm kd}}\right)^{9/16} \tag{34}$$

Note that since $T_\chi \propto a^{-9/8}$ before reheating, b_v as defined this way is in fact a constant. Since b_v is indeed a constant, and $T_\chi(a) = T_\chi^A(a)$ for $a \le 0.1a_{\rm RH}$, we can substitute $T_\chi(a)$ for $T_\chi^A(a)$ and evaluate b_v at $a = 0.1a_{\rm RH}$, finding that

$$b_v = \left(\frac{T_\chi^A(0.1a_{\rm RH})}{T_{\rm kd}}\right)^{1/2}\left(\frac{0.1a_{\rm RH}}{a_{\rm kd}}\right), \tag{35}$$

where $a_{\rm kd}$ comes from Eq. (28). We introduce a new prefactor d_v^2 to the definition of $T_\chi(a)$ in Eq. (32) to assuage the ambiguity from $T_\chi \sim v_\chi^2 m_\chi$. With the above form for b_v and the addition of the new d_v parameter, we can now solve T_χ at $a > a_v$ for a_v, using the constraint from Eq. (33) to replace $T_\chi(a)$ for $a \gg a_{\rm RH}$, finding:

$$a_v = \left[\frac{1.37 T_\chi^A(a_{\rm RH}) a_{\rm RH}^2}{d_v^2 b_v^2 T_{\rm kd} a_{\rm kd}^{9/8}}\right]^{8/7}. \tag{36}$$

We can now combine all of this for our final model, which only depends on our temperatures, c_χ, and our fit parameter d_v:

$$\frac{k_{\rm cut}}{k_{\rm RH}} = \left[\frac{b_v d_v}{b_H}\frac{c_\chi}{\sqrt{2}r}\left(\frac{T_{\rm RH}}{T_{\rm kdS}}\right)^{5/2}\left(\frac{2}{5}\right)^{3/8}\left(\frac{a_{\rm RH}}{a_{\rm Ht}}\right)^{\frac{25}{16}} \times \left\{16\left(\left(\frac{a_{\rm Ht}}{a_{\rm kd}}\right)^{\frac{1}{16}} - 1\right) + \frac{16}{7}\left(\left(\frac{a_v}{a_{\rm Ht}}\right)^{\frac{7}{16}} - 1\right) + \boxed{\left(\frac{a_v}{a_{\rm Ht}}\right)^{\frac{7}{16}} \ln\left(\frac{a_f}{a_v}\right)}\right\}\right]^{-1} \tag{37}$$

Using transfer function data for $a_f = 100a_{\rm RH}$ at fixed $T_{\rm kdS}/T_{\rm RH}$, we fit the model to determine d_v. At the same temperature ratio, we then use the completed model with the d_v fit at $a_f = 100a_{\rm RH}$ to predict $k_{\rm cut}/k_{\rm RH}$ at $a_f = 200a_{\rm RH}$, $500a_{\rm RH}$, and $1000a_{\rm RH}$ compared to those from KDEMDE. This allows us to draw an interesting conclusion: using only the d_v fit from the KDEMDE data at $a_f = 100a_{\rm RH}$ across many values of c_χ, we find that as a_f increases, the difference between our model and the numerical KDEMDE value of $k_{\rm cut}/k_{\rm RH}$ decreases. This is remarkable, as it implies that were we to evolve perturbation modes out to a_0 using KDEMDE, the model would be able to accurately predict the free-streaming cut-off mode. The late-time constraint on the temperatures from Eq. (33) is accounted for in a_v and ensures that we accurately capture the temperature evolution at late times. This is important because the integral to calculate $\lambda_{\rm fs}$ is dominated by the contribution from late times, which is encoded in the boxed, logarithmic term in Eq. (37).

Unfortunately, the values of d_v from fits of the $k_{\rm cut}/k_{\rm RH}$ vs. c_χ relationship do not agree across different temperature ratios. Note that a_v depends on both b_v and d_v. While fitting data from KDEMDE for d_v,

TABLE I. Comparison between the fit parameter d_v for the two different functional forms of b_v. The column labeled "Early d_v" shows fit values of d_v with b_v defined in Eq. (35). The column labeled "Late d_v" shows fit values of d_v with b_v as defined in Eq. (39). The fits were made against the $k_{\rm cut}/k_{\rm RH}$ vs. c_χ relationship data from KDEMDE taken at $a_f = 100 a_{\rm RH}$. The reduced fluctuation in d_v for the late-time dependent b_v of Eq. (39) demonstrates that this form of b_v matches the temperature dependence better.

$T_{\rm kdS}/T_{\rm RH}$	Early d_v	Late d_v
2	1.350	1.024
3	1.259	1.035
4	1.268	1.066

we find that the model fits best for d_v values that push $a_v/a_{\rm RH}$ to high values upwards of 40. The large $a_v/a_{\rm RH}$ ratio indicates that the model is artificially suppressing the first two additive terms in Eq. (37) in favor of the third, boxed term of our piecewise integral of $\lambda_{\rm fs}$. This suggests that the post-reheating behavior dominates the calculation of $k_{\rm cut}/k_{\rm RH}$. This motivates us to make a remarkable simplification to the model. Since the late-time behavior dominates the calculation of $k_{\rm cut}/k_{\rm RH}$, the first two terms in Eq. (37) become negligible compared to the third term as a_f increases. Therefore, we choose to simply drop the first two terms. We set $a_v = a_{\rm RH}$ and consider the model:

$$\frac{k_{\rm cut}}{k_{\rm RH}} = \left[\frac{b_v d_v}{b_H}\frac{c_\chi}{\sqrt{2}r}\left(\frac{T_{\rm RH}}{T_{\rm kdS}}\right)^{5/2}\left(\frac{2}{5}\right)^{3/8}\left(\frac{a_{\rm RH}}{a_{\rm Ht}}\right)^{\frac{25}{16}}\times \left\{\left(\frac{a_{\rm RH}}{a_{\rm Ht}}\right)^{\frac{7}{16}}\ln\left(\frac{a_f}{a_{\rm RH}}\right)\right\}\right]^{-1} \tag{38}$$

where d_v now functions as the overall normalization parameter and we express b_v in terms of $a_v = a_{\rm RH}$ by solving Eq. (36) for b_v:

$$b_v = \sqrt{\frac{1.37 T_\chi^A(a_{\rm RH}) a_{\rm RH}^2}{a_{\rm RH}^{7/8} T_{\rm kd} a_{\rm kd}^{9/8}}} \tag{39}$$

This formulation of b_v incorporates our late-time constraint from Eq. (33). With the simplified model in Eq. (38), we can go back to fitting data in the $k_{\rm cut}/k_{\rm RH}$ vs. c_χ relationship such as in Fig. 9. With $a_v = a_{\rm RH}$ and only one free parameter d_v, we can now compare the two different definitions of b_v in Eqs. (35) and (39). We fit the simplified model to the $k_{\rm cut}/k_{\rm RH}$ vs. c_χ data for multiple temperature ratios and display the fitting parameters in Table I.

Table I shows a strong improvement of the model by using the one-part integral and b_v defined in Eq. (39). The reduced fluctuation in the near-unity fitting parameter with this definition of b_v shows that the functional form of b_v better captures the temperature dependence at late times than that of Eq. (35). As demonstration of the predictive power of the model under this new formulation, in Figure 10 we look at the time evolution

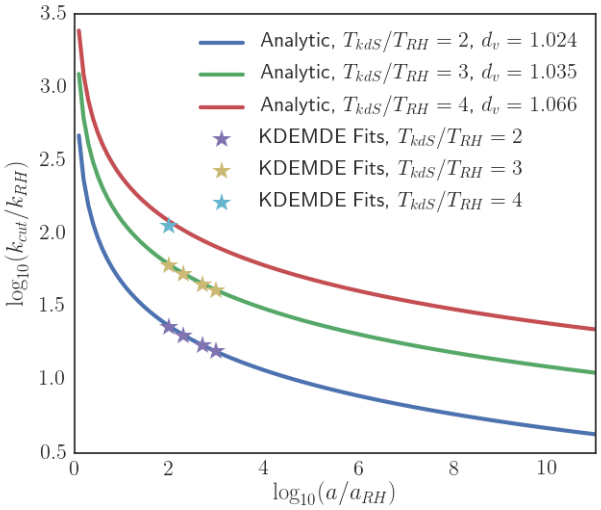

FIG. 10. For fixed $c_\chi = 0.1$, we use the analytical model in Eq. (38) with b_v as defined in Eq. (39) to predict the time evolution of $k_{\rm cut}/k_{\rm RH}$. For several temperature ratios, we compare this time evolution to that found via KDEMDE for the corresponding sets of parameters. The ratios are extrapolated out to $a_{\rm eq} \sim 10^{10} a_{\rm RH}$.

of $k_{\rm cut}/k_{\rm RH}$ for several temperature ratios and compare to the time evolution from KDEMDE. This figure highlights the expected logarithmic decrease of $k_{\rm cut}/k_{\rm RH}$ with a_f. When assessing temperature ratios greater than 4, we have no data from KDEMDE to make a fit for d_v. Fortunately, as demonstrated by the "Late d_v" column of Table I, the fit parameter is nearly constant across temperature ratios. For this reason, predictions made for $T_{\rm kdS}/T_{\rm RH} > 4$ can be made using the d_v fit from $T_{\rm kdS}/T_{\rm RH} = 4$ with minimal loss in accuracy due to fluctuations in d_v.

Since we have completed our model fitting by considering $a_f \ll a_{\rm eq}$, we can now incorporate the final term in the model that is evaluated from $a_{\rm eq}$ to a_0. Once matter domination begins, the Hubble rate becomes:

$$H(a) = b_H\left(\frac{k_{\rm RH}}{a_{\rm RH}}\right)\left(\frac{a_{\rm Ht}}{a_{\rm eq}}\right)^2\left(\frac{a_{\rm eq}}{a}\right)^{3/2} \qquad a \geq a_{\rm eq}. \tag{40}$$

However, the dark matter velocity remains unchanged from Eq. (27). We evaluate the integral in Eq. (24) as previously done out to $a_{\rm eq}$, with the simplified model in Eq. (38). However, we now add an additional term resulting from the evaluation of the integral from $a_{\rm eq}$ to a_0, such that $k_{\rm cut}/k_{\rm RH}$ evaluated today is:

$$\frac{k_{\rm cut}}{k_{\rm RH}} = \left[\frac{b_v d_v}{b_H}\frac{c_\chi}{\sqrt{2}r}\left(\frac{T_{\rm RH}}{T_{\rm kdS}}\right)^{5/2}\left(\frac{2}{5}\right)^{3/8}\left(\frac{a_{\rm RH}}{a_{\rm Ht}}\right)^{\frac{25}{16}}\times \left\{\left(\frac{a_{\rm RH}}{a_{\rm Ht}}\right)^{\frac{7}{16}}\ln\left(\frac{a_{\rm eq}}{a_{\rm RH}}\right) + 2\left(\frac{a_{\rm RH}}{a_{\rm Ht}}\right)^{7/16}\left(1-\sqrt{\frac{a_{\rm eq}}{a_0}}\right)\right\}\right]^{-1}. \tag{41}$$

The contribution to this calculation from the period between matter-radiation equality and today is dwarfed by the contribution between reheating and matter-radiation equality. Now that we are comfortable with our model, we can determine the temperature at c_χ parameters that will provide this sufficiently high $k_{\rm cut}/k_{\rm RH}$ at a_0. In order to generate a dark matter annihilation boost sufficient to overcome the reduced annihilation cross section, we need at least $k_{\rm cut}/k_{\rm RH} \approx 20$ [11]. Figure 11 shows the parameter space of the temperature ratio and c_χ that have $k_{\rm cut}/k_{\rm RH} \geq 20$ at a_0. Dark matter particles with $m_\chi/T_{\rm RH}$ in the range 100 to 200 are most capable of having their annihilation rate boosted above the current minimum sensitivity threshold of missions such as the *Fermi Gamma-Ray Telescope*. Since dark matter typically freezes out before it kinetically decouples, we must also demand that the freeze-out temperature T_f be greater than $T_{\rm kd}$. According to Ref. [11], dark matter typically freezes out when $m_\chi \sim 10T$. This demands that $T_f/T_{\rm RH} \sim 0.1 m_\chi/T_{\rm RH}$.

Unfortunately, $T_{\rm kdS}/T_{\rm RH} = 6$ is the lowest temperature ratio that gives $k_{\rm cut}/k_{\rm RH} \approx 20$ at a_0 for $m_\chi/T_{\rm RH} \leq 200$. In this case, $T_{\rm kd} \approx 9T_{\rm kdS} \approx 54T_{\rm RH}$. For our upper bound $m_\chi/T_{\rm RH} = 200$, we have that $T_f/T_{\rm RH} \approx 20$. Clearly, $T_{\rm kd} > T_{\rm f}$, which is not consistent with the standard theories of dark matter formation. The other possible scenario that would provide $k_{\rm cut}/k_{\rm RH} \approx 20$ at a_0 with a lower temperature ratio that remains consistent with standard theories would require that $m_\chi/T_{\rm RH} \gg 200$, resulting in heavy suppression of the annihiliation cross section that would push dark matter annihiliations below the observable threshold for any mission in the near future [11]. We are interested in studying the scenario where the EMDE could have potential constraining power on the dark matter particle, and thus we will choose our parameters to be $T_{\rm kdS}/T_{\rm RH} = 6$ and $c_\chi = 0.245$. With these parameters, we can generate a matter power spectra with the necessary $k_{\rm cut}/k_{\rm RH} = 20$, to be done in the next section.

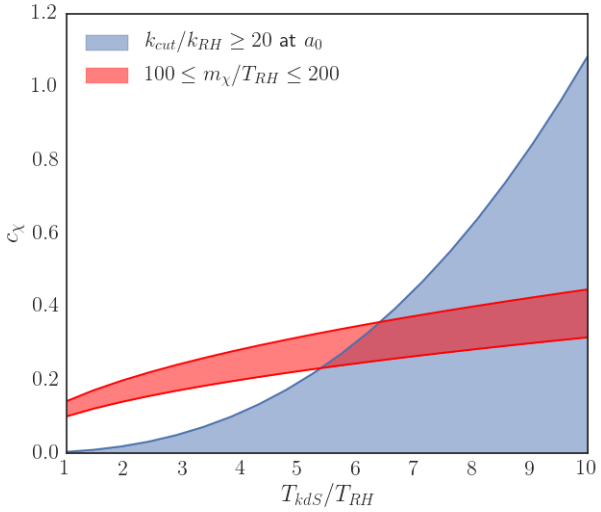

FIG. 11. Using the model of $k_{\rm cut}/k_{\rm RH}$ from Eq. (38) and the converged $b_v = 1.770$ from Eq. (39), we find the maximum value of c_χ for each temperature ratio that will provide a $k_{\rm cut}/k_{\rm RH} \geq 20$ at a_0. This is compared to the desired parameter space of $100 \leq m_\chi/T_{\rm RH} \leq 200$. Note that for a given temperature ratio, a lower c_χ corresponds to a higher $m_\chi/T_{\rm RH}$.

III. COSMOLOGICAL SIMULATIONS

In this section, we study the evolution of a universe that undergoes an EMDE with $k_{\rm cut}/k_{\rm RH} = 20$. We start out by generating the matter power spectrum for this universe that represents the enhanced perturbations on modes $k_{\rm RH} < k < k_{\rm cut}$. This power spectrum will be transformed into initial condition data for the `GADGET-2` cosmological N-body simulator code [13]. We run the simulation at multiple scales in order to study a larger range of masses and confirm convergence between the simulations. The N-body simulator returns only the phase-space data of all particles in the code. This particle data is piped through the `Rockstar` [16] halo finder to determine the location and radius of all gravitationally-bound structures in the simulation. We employ the convention that the halo radius is that which makes the average halo density $\rho_{\rm halo} = 200\rho_c$, where ρ_c is the critical density of the universe.

With these halo catalogs collected, we can determine some macroscopic statistics about the halo populations from the simulation. The halo mass function describes the number density of dark matter halos per mass interval $dn/d\ln M$. We compare these results to the Press-Schecter [18] and Sheth-Tormen [17] formalisms.

We then briefly discuss the total bound matter fraction in the simulation as a function of redshift z. As time progresses, we expect that the total amount of matter bound into structure will increase. This can be verified by generating a halo catalog for each simulation snapshot and determining the total mass in structure compared to the total mass simulated in the box. Similarly, we look at the total fraction of matter bound in substructure per halo as a function of host halo mass.

We then proceed to study the microscopic properties of the simulations, namely the individual microhalos. We employ visualization routines from the `MayaVi` [24] Python module to verify the halo center identification accuracy of the halo catalogs. The `Rockstar` halo finder keeps track of the halo structure hierarchy, identifying subhalos of each host halo. This tree-level hierarchy represents the merger history of the microhalos. With this hierarchy, we visually study the levels of substructure present in the largest host halos from the simulations. Afterward, we shift our focus to the density profile, a function that describes the density as a function of radius with respect to the halo center. Using the particle data from a halo, we can calculate the numerical density

profile and fit it against the generalized Navarro-Frenk-White (NFW) profile [19]. To calculate the halo boost factor of each halo as in Eq. (1), we use the NFW profile for a standard reference halo in a process described in Subsection III E. We conclude this section with all the necessary groundwork laid to calculate the boost factor of every halo in the simulation and continue forward by analyzing the statistical properties of these boosts.

Many of the aforementioned processes are repeated for an identical universe that still has a free-streaming cut-off scale but lacks an EMDE. See the "Only FS cut-off" curve in Fig. 12. These "standard" simulations serve as a useful control to demonstrate the boost due to the EMDE in the EMDE simulations.

A. Power Spectra and Simulation Parameters

With an enhanced region of wavenumber-space now determined such that $k_{\rm cut}/k_{\rm RH} = 20$, we create a power spectrum for a universe that undergoes an EMDE and reheats at $T_{\rm RH} = 30$ MeV. This power spectrum is related to the transfer function of each individual mode according to Eq. (19), where the primordial power spectrum $\tilde{P}(k)$ comes from observations of the cosmic microwave background. The other component of the power spectrum, the transfer function $T_{z_i}(k)$, is calculated using the collisionless Boltzmann equation by determining the density perturbation of each wavenumber at the starting redshift of the simulation, as in Subsec. II E. This power spectrum is used as the input to the `UniGrid` routine, which randomly generates density perturbations $\delta_\chi(\vec{x}, z_i)$ that obey the statistical properties demanded by the power spectrum. Here, the z_i simply indicates that the perturbations are at the initial redshift where the N-body simulation begins the evolution. This $\delta_\chi(\vec{x}, z_i)$ data is then piped through `Delta2Particles`, which generates the initial coordinate and momentum data for all the particles in the simulation. The `GADGET-2` N-body simulator takes this initial particle configuration and simulates the gravitational evolution up until a desired final redshift. Throughout this work, we use the cosmological parameters $h = 0.678$, $\Omega_m = 0.309$, $\Omega_b = 0.049$, and $\Omega_\Lambda = 0.691$ in accordance with the 2015 results from *Planck* [12].

In order to study the evolution of microhalos with an N-body simulation, we must be diligent to ensure that the mass resolution of the simulation is sufficient to resolve the microhalos. The EMDE only alters structure on mass scales below the reheat mass $M_{\rm RH}$, which is the mass enclosed in the Hubble radius at reheating. The Hubble radius $R = 1/(aH)$, and $k \approx R^{-1}$ up to order unity. Therefore, the mass enclosed in the Hubble radius at reheating is

$$M_{\rm RH} = \frac{4}{3}\pi\rho_m R_{\rm RH}^3 = \frac{4}{3}\pi\rho_m k_{\rm RH}^{-3}. \tag{42}$$

Since $k_{\rm RH}$ is a comoving quantity, ρ_m is simply the matter density today. A convenient expression for the reheat mass in terms of the reheat temperature is:

$$M_{\rm RH} = 32.7 M_\oplus \Big(\frac{10\ {\rm MeV}}{T_{\rm RH}}\Big)^3 \Big(\frac{g_{*s}[T_{\rm RH}]}{10.75}\Big)\Big(\frac{10.75}{g_*[T_{\rm RH}]}\Big)^{3/2}. \tag{43}$$

The two key simulation parameters that determine the individual particle mass are the particle count and the box size. The number of CPU hours required to complete a simulation roughly scales with the particle count, and for this reason we choose $N_{part} = 1024^3$ particles such that each simulation takes on the order of 10^4 CPU hours. We select small box sizes of $(30\ {\rm pc}/h)^3$, $(60\ {\rm pc}/h)^3$, and $(120\ {\rm pc}/h)^3$. These simulation configurations result in particle masses of $2.16\times10^{-12}\ M_\odot/h$, $1.73\times10^{-11}\ M_\odot/h$, and $1.38\times10^{-10}\ M_\odot/h$, respectively. The combination of large particle count and small box size allows us to probe a rather low mass regime. We briefly note that we also employ an even smaller $1\ ({\rm pc}/h)^3$ simulation exclusively to study high resolution density profiles. See Subsection III E for our discussion on this topic.

The `Rockstar` halo finder only catalogs halos above a certain minimum particle count, which we select to be 100 particles. Therefore, our 30 pc/h simulation has a minimum halo mass of $2.16 \times 10^{-10}\ M_\odot/h$. Referring back to Eq. (43), we see that for a reheat temperature of $T_{\rm RH} = 30$ MeV, the reheat mass is $M_{\rm RH} = 3.5 \times 10^{-6}\ M_\odot$, or approximately one Earth-mass. For this same reheat temperature, the smallest microhalos that can form will be at the free-streaming cut-off mass limit, $M_{\rm cut} = 4 \times 10^{-10}\ M_\odot$. This is clear from Eq. (42),

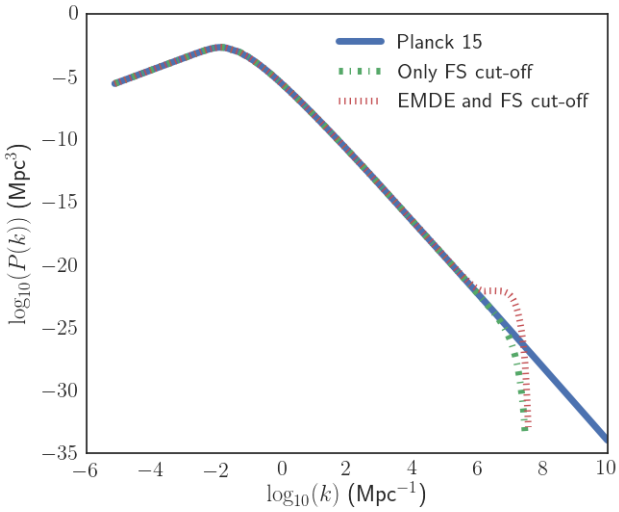

FIG. 12. The matter power spectrum at $z = 500$: the solid curve extrapolates results from the Planck 2015 mission [12]; the dash-dotted curve uses the same data from Planck but contains a free-streaming cutoff with $k_{\rm cut}/k_{\rm RH} = 20$ in a universe with reheating at $T_{\rm RH} = 30$ MeV; the dotted curve is the power spectrum of a universe with an EMDE, where the enhanced region rises above the standard power spectrum for modes bounded by $k_{\rm RH}$ and $k_{\rm cut}$.

considering $k_{\rm cut}/k_{\rm RH} = 20$, the cut-off mass is a factor of 20^3 smaller than the reheat mass.

This low reheat temperature was chosen so that we could resolve microhalos in the mass regime $M_{\rm cut} < M < M_{\rm RH}$ for our given simulation parameters. A higher reheat temperature will push the microhalo formation to increasingly small mass regimes that are more inaccessible to an N-body simulator. However, it is important to recall from Section II that only the ratio $T_{\rm kdS}/T_{\rm RH}$ affects the transfer function and thus the power spectrum. The primordial microhalos will form at approximately the same redshift regardless of the reheat temperature, with formation time only depending on $k_{\rm cut}/k_{\rm RH}$. For a fixed ratio of $k_{\rm cut}/k_{\rm RH}$, the first microhalos to form will all have approximately the same density, whereas the size of the microhalo clumps will depend on $T_{\rm RH}$. Ref. [11] demonstrates that regardless of reheat temperature, the differential bound mass fraction $df/d\ln M$ remains fixed relative to the reheat mass. With this fixed relative differential bound mass fraction and the consideration that all primordial microhalos form at the same density, we expect the annihilation boost to not be sensitive to $T_{\rm RH}$. Therefore, the following results are general to higher reheat temperatures.

In order to capture the formation of low-mass microhalos in the simulation, the EMDE simulations begin at a $z_i = 2000$. Since this redshift is fairly near the point of matter-radiation equality, effects due to radiation are still significant. Unfortunately, `GADGET-2` does not presently have radiation physics incorporated, and thus we are unable to model the effects due to radiation. To mitigate this, the input power spectra are generated for $z = 500$, where radiation effects are negligible, and integrated back to $z_i = 2000$ assuming only that the Universe is entirely matter-dominated. This way, when the simulation evolves from a redshift of 2000 to 500, the power spectrum will be accurate at $z = 500$, and the remaining evolution of the simulation can continue forward without the need for radiation physics. The simulations that evolve without an EMDE but with a free-streaming cut-off begin at $z_i = 500$. The N-body simulator evolves the code up to $z_f = 30$ and takes 10 snapshots of the particle data along the way at equally-spaced intervals in scale factor. These snapshots will be used to study the total bound mass fraction in Subsection III C.

B. Halo Mass Functions

The majority of our subsequent analysis focuses on the final snapshot data from `GADGET-2` at $z_f = 30$. This particle data is sent through `Rockstar` to find all halos of particle count greater than 100. We are interested in verifying the microhalo populations of our simulations against established theory. The Press-Schecter mass function [18] is an analytical formalism that predicts the number density of halos as a function of mass interval, defined as:

$$\frac{dn}{d\ln M} = \sqrt{\frac{2}{\pi}}\frac{\rho_m \delta_c}{M\sigma(M,z_f)}\exp\Big[-\frac{\delta_c^2}{2\sigma(M,z_f)}\Big]\Big|\frac{d\ln\sigma}{d\ln M}\Big| \tag{44}$$

where $\delta_c = 1.686$ for $z \gtrsim 2$ is the critical linear overdensity, ρ_m is the matter density of the Universe today, and $\sigma(M,z_f)$ is the rms density perturbation in a sphere that contains a mass M:

$$\sigma^2(M,z) = \int \frac{d^3k}{(2\pi)^3}[D(k,z)T(k)]^2 P_p(k) F^2(kR) \tag{45}$$

where $D(k,z)$ is the scale-dependent growth function [5], $T(k)$ is the transfer function, $P_p(k)$ is the power spectrum of super-horizon density perturbations during radiation domination, and

$$F(kR) = \exp\Big[-\frac{k^2(\alpha R)^2}{2}\Big] \times \frac{2[\sin(kR) - (kR)\cos(kR)]}{(kR)^3} \tag{46}$$

with $\alpha = 0.0001$ and $R = [3M/(4\pi\rho_m)]^{1/3}$ (Refs. [11] and [5]).

A similar model of the halo mass function was constructed by Sheth & Tormen [17]:

$$\frac{dn}{d\ln M} = 0.3222 \times \frac{\rho_m}{M}\Big|\frac{d\ln\sigma}{d\ln M}\Big|\sqrt{\frac{2}{\sqrt{2}\pi}} \times\Big[1+\Big(\frac{\sqrt{2}\sigma(M,z_f)}{\delta_c^2}\Big)^{0.3}\Big]\frac{\delta_c}{\sigma(M,z_f)}\exp\Big[-\frac{\sqrt{2}\delta_c^2}{4\sigma^2}\Big] \tag{47}$$

In order to calculate the mass functions from the numerical data, we extract from the Rockstar halo catalog an array of the masses of all **host** halos, namely only the ones that have no parent halo in the substructure tree. Then, the halos are binned by mass using an adaptive binning routine so that for a simulation with $N_{\rm h,tot}$ hosts, the minimum number of halos in a bin is

$$N_{min} = 10.54\ln(N_{\rm h,tot}) - 40.36. \tag{48}$$

The bins are automatically widened by small $\delta\ln M$ in order to satisfy the requirement. In Figure 13, we plot the numerical mass functions from all of the 1024^3 particle simulations and compare them to the Press-Schecter and Sheth-Tormen mass functions. The benefit to running identical simulations at increasing box sizes becomes clear: the small box simulations probe the smallest mass regimes whereas the larger box simulations probe larger mass regimes. The figure demonstrates convergence between the simulations, indicated by the overlap of the mass functions for the $(30\ {\rm pc}/h)^3$, $(60\ {\rm pc}/h)^3$, and $(120\ {\rm pc}/h)^3$ simulations. We compare the simulations that evolved with an enhanced power spectrum due to the EMDE with identical simulations that were not enhanced by an EMDE. The increased halo number density in the mass regime $M < M_{\rm RH}$ is quite noticeable for the EMDE simulations. Above the reheat mass, we see the mass

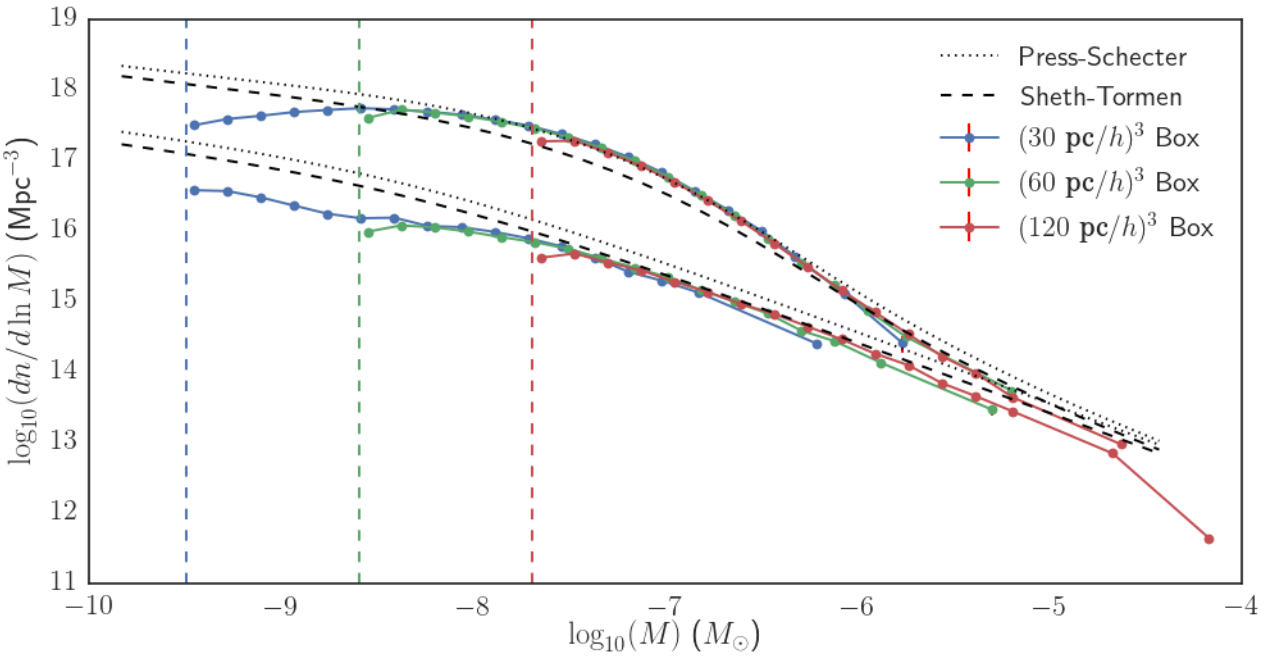

FIG. 13. Comparison between mass functions from numerical simulations and the predictions made by the Press-Schecter (Eq. (44)) and Sheth-Tormen (Eq. (47)) mass functions. The numerical data is taken at $z_f = 30$ for six different 1024^3 particle simulations. The three numerical curves that are of larger magnitude in $dn/d\ln M$ correspond to the EMDE simulations, whereas the lower magnitude curves correspond to the standard simulation without an EMDE. The vertical lines correspond to the minimum halo size of 100 particles for the corresponding simulation. Note that the standard and EMDE mass functions are nearly converged at the reheat mass $M_{\rm RH} = 3.5 \times 10^{-6}\ M_\odot$. The enhanced level of structure formation due to the EMDE is clear from the large difference in $dn/d\ln M$ between $M_{\rm cut} < M < M_{\rm RH}$.

functions begin to converge such that the EMDE plays no role in higher mass structure formation, and this is indeed confirmed by the numerical mass functions. The figure also demonstrates that the simulation results are reasonable, as the mass functions are in fairly good agreement with the analytical predictions. We find that the Press-Schecter mass function is a better predictor of microhalo number density in the EMDE simulation, whereas the Sheth-Tormen mass function is a more accurate model of the microhalo number density for a universe that evolves in the absence of an EMDE. The Press-Schecter mass function considers spherical collapse of dark matter halos whereas the Sheth-Tormen mass function considers elliptical collapse. The stronger agreement between the Press-Schecter mass function and the results from the EMDE simulation suggests that structure collapse could be more spherical for EMDE-generated microhalos. We now shift our attention to subhalo mass statistics and the evolution of the total bound matter fraction with redshift.

C. Bound Matter Fraction and Substructure Mass Fraction

For a given halo, its substructure mass fraction f_s is defined as the total amount of mass bound in subhalos relative to the total mass in the host halo:

$$f_s = \frac{\sum_i M_{\rm sub,i}}{M_{\rm host}} \tag{49}$$

where i runs over all subhalos, $M_{\rm sub,i}$ is the mass of a particular subhalo, and $M_{\rm host}$ is the total mass of the host halo. We are interested in the statistical properties of this quantity as a function of host halo mass.

In Figure 14, we study the substructure mass fraction across several redshifts and compare the result at $z_f = 30$ between the EMDE simulation and the standard radiation-dominated simulation. As expected, there are substantially more total host halos in the EMDE simulation at z_f than there are in the standard simulation. In fact, the difference is about a factor of 42, with approximately 106,000 hosts in the EMDE simulation and only 2,500 in the standard simulation. This is readily apparent from the aforementioned halo mass functions. As the EMDE simulation evolves, we can see that higher mass host halos begin to contain substructure. At high redshift, the majority of halos have $f_s = 0$. We also see that the total number of substructure-less host halos decreases as time increases. In particular, at $z = 186$, over 96% of halos contain no substructure. By $z_f = 30$, only 85% of halos contain no substructure. This indicates that as the halos evolve, they begin to merge and form larger, substructure-rich host halos. Interestingly, the number

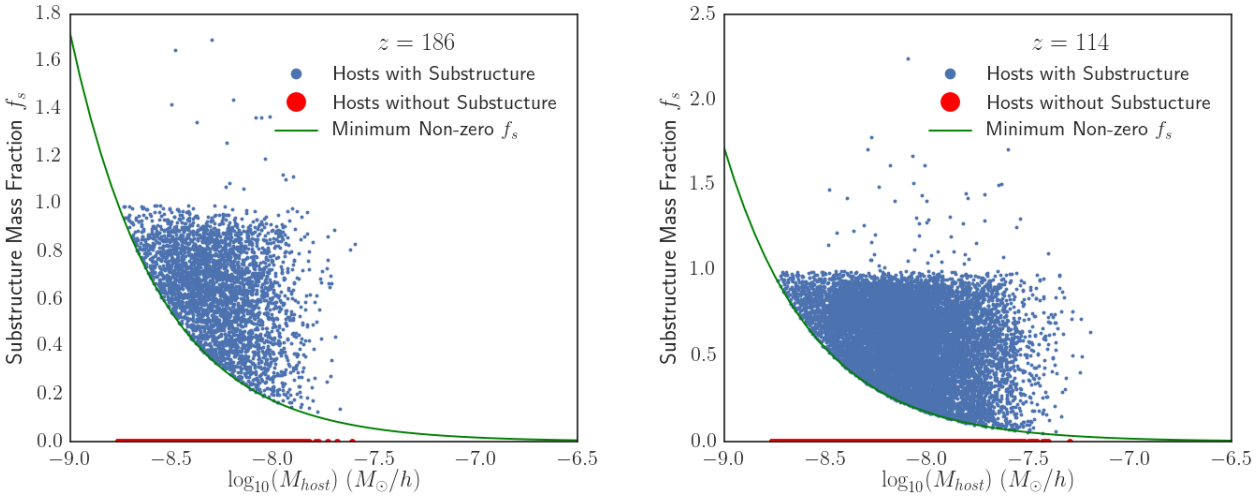

(a) Redshift evolution of the substructure mass fraction for a universe that undergoes an EMDE. At $z = 186$, over 96% of halos contain no substructure. By $z = 114$, only 91% of halos contain no substructure.

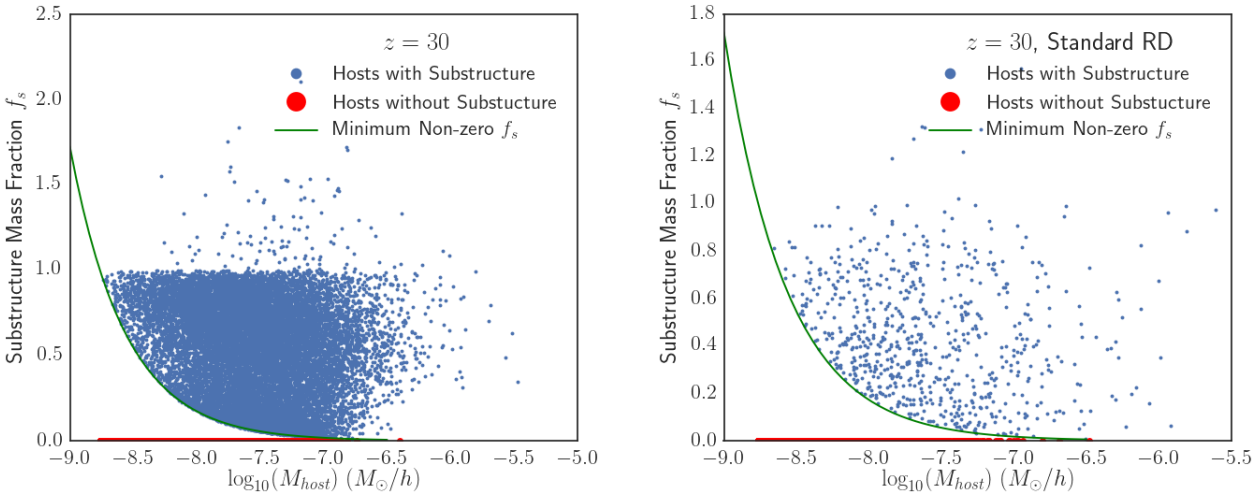

(b) On left: continued redshift evolution of EMDE simulation. By $z = 30$, 85% of halos contain no substructure. On right: When contrasted against a simulation that undergoes standard radiation domination, only 71% of halos contain no substructure at $z = 30$. However, hosts are substantially more abundant in the EMDE simulation by a factor of 42.

FIG. 14. Substructure mass fractions for a 1024^3 particle, 60 $(\mathrm{pc}/h)^3$ box simulation. The first three images depict redshift evolution and the final image compares the results at $z_f = 30$ between the standard simulation and the EMDE simulation. The green curve represents the minimum possible fraction that one single 100 particle subhalo can contribute to the total host halo mass. Fractions greater than 1 are possible due to `Rockstar`'s subhalo identification technique: only the center of a subhalo must be within the host halo R_{200} radius.

of total host halos increases temporarily and then begins to decrease after the sub-reheat mass halos stop forming and begin to merge. At $z = 186$, there were 76,000 hosts, which increases up to 140,000 by $z = 114$. However, these microhalos begin to merge and by $z_f = 30$ there are only 106,000 host halos. We expect that this trend would continue if lower redshifts were probed. The general trend from Fig. 14 is that as the more massive halos begin to form, they do so by merging with smaller halos. At first glance, the data in Fig. 14 appears quite dense and could be masking a trend. However, after inspection with a Hess diagram, we report that there is no trend for f_s versus M_{host}. Unfortunately, the simulation resolution limits our ability to fully study this relationship. In order for `Rockstar` to identify a subhalo within a host halo, the subhalo itself must contain at least 100 particles. The curves in Fig. 14 track the value of f_s for a given host halo mass that corresponds to the host containing one subhalo with the minimum of 100 particles. It is quite possible that some of the low-mass halos could

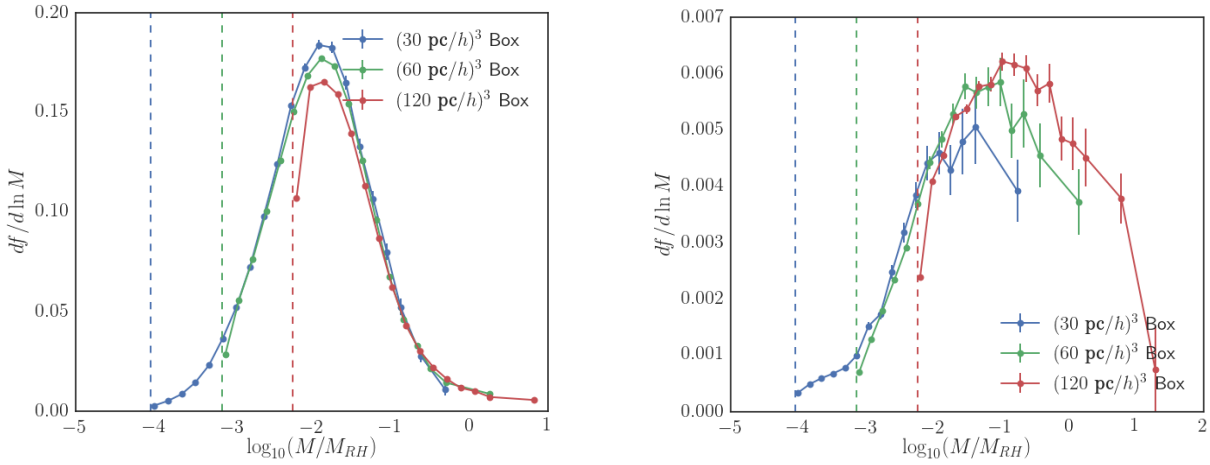

FIG. 15. The differential bound fraction given by Eq. (50) at $z_f = 30$. On left: $df/d\ln M$ from the EMDE simulations. On right: $df/d\ln M$ from the standard simulations. Note the large boost in $df/d\ln M$ due to the EMDE as compared to the standard simulation.

have substructure that is not resolved by the simulation. If a higher resolution was used, it may be possible to further explore the $f_s - M_{\rm host}$ relationship in search of a trend.

We now introduce the differential bound fraction of dark matter. Recall that the halo mass function is $dn/d\ln M$ and describes the dark matter number density as a function of mass bin. The differential bound fraction describes the fraction of the total dark matter that is bound into a particular mass bin. We denote this quantity $df/d\ln M$ and it follows directly from the mass function:

$$\frac{df}{d\ln M} = \frac{dn}{d\ln M} V_{\rm box} \frac{M}{M_{\rm box}} \tag{50}$$

with $M_{\rm box} = N_{\rm sim} M_p$. Here, M_p is the mass of a particle and $N_{\rm sim} = 1024^3$ particles in the simulation. Note that $\frac{dn}{d\ln M} V_{\rm box} = \frac{dN}{d\ln M}$, the differential halo count per mass bin. Clearly, the factor of $M/M_{\rm box}$ transforms this quantity into a mass fraction, with M located at the center of each corresponding mass bin. Since we have already calculated our mass functions $dn/d\ln M$ in Subsec. III B, it is simple to calculate $df/d\ln M$. In Fig. 15, we plot the differential bound fraction for both the EMDE and standard simulations. This result is consistent with predictions from Press-Schecter [18]. The differential bound fraction of a universe that evolved with an EMDE peaks at approximately $M/M_{\rm RH} \approx 10^{-2}$ at $z = 30$. We also see that, as expected, $df/d\ln M$ is substantially lower for the standard simulation. Note that the level of disagreement between the three different box sizes is in fact quite small and only due to resolution effects. When compared with the great convergence seen between the various mass functions of Fig. 13, we point out that the mass functions were plotted in logarithmic space, whereas $df/d\ln M$ is only in linear space. Therefore, any lack of convergence due to resolution in the mass functions is obscured where it is otherwise apparent in $df/d\ln M$. Nonetheless, we are satisfied with the level of convergence demonstrated.

Of particular interest is the integral of $df/d\ln M$ up to the reheat mass, namely the total bound fraction in sub-reheat mass halos:

$$f_{\rm tot}(z_f) = \int_{\ln M_{\rm cut}}^{\ln M_{\rm RH}} \frac{df}{d\ln M}\Big|_{z_f} d\ln M. \tag{51}$$

We are interested in the total bound fraction as a function of redshift. Rather than numerically integrate the $df/d\ln M$ curves from Fig. 15, $f_{\rm tot}$ can be calculated directly from the `Rockstar` halo catalogs with:

$$f_{\rm tot} = \frac{\sum_i^{M<M_{\rm RH}} M_{\rm host,i}}{M_{\rm box}} \tag{52}$$

where i runs over all host halos with mass below the reheat mass as identified by `Rockstar` and $M_{\rm host,i}$ is the mass of each host. Analytical models of an EMDE predict that the fraction of dark matter bound in microhalos may increase by several orders of magnitude for a reheat temperature as low as $T_{\rm RH} = 30$ MeV when compared to structure formation in the absence of an EMDE [11]. Figure 16 demonstrates the redshift evolution of $f_{\rm tot}$ for both a universe that experiences an EMDE and a standard universe. As predicted, the fraction of dark matter that is bound in microhalos is substantially higher due to an EMDE at nearly 70% at $z_f = 30$. Ideally, we wish to calculate $f_{\rm tot}$ at lower redshifts. This is unfortunately not possible since our simulation stops at $z_f = 30$. We expect to see that as redshift decreases, the total matter fraction bound into microhalos will decrease as microhalos begin to merge into larger hosts of mass greater than $M_{\rm RH}$ and many microhalos are destroyed by tidal stripping. With these macroscopic properties of our simulations verified, we continue onwards to study individual microhalos and their substructure.

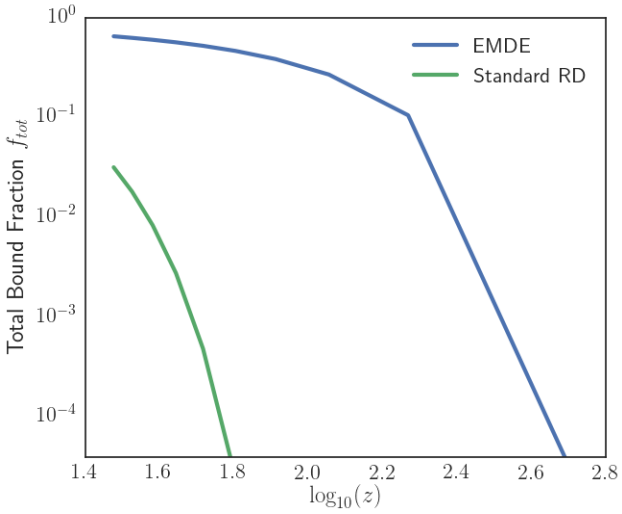

FIG. 16. Comparison between the fraction of matter bound into microhalos for a standard radiation-dominated universe and a universe that experiences an EMDE. Simulation parameters: $(60\ \mathrm{pc}/h)^3$ box, 1024^3 particles.

D. Halo Visualization and Substructure Analysis

In this subsection, we use visualization tools from the `MayaVi` Python module to visualize the evolution and structure of individual halos in our simulations. We also utilize the substructure tree data from the halo catalogs to identify substructure.

We expect that primordial microhalos will begin forming by a redshift $z \approx 200$ as a consequence of an EMDE. To confirm this, we visualize the evolution of a large host halo in Figure 17. We begin by selecting the largest host halo at $z_f = 30$ in the EMDE simulation. We use the halo center coordinates and radius to collect all particles from the `Rockstar` particle data files. These particles are then binned into a three-dimensional mesh. The particle counts inside each bin are representative of the density at that point in the halo. We then sum the bin counts along one axis to collapse the data into a two-dimensional array. This array is visualized as a heatmap using `MayaVi`. Since we are interested in the halo evolution, we repeat the preceding procedure for each `GADGET-2` snapshot, continuing to use the location and size of the final host halo. The density of each heatmap is set on the same scale such that the most dense point of the final host halo from the EMDE simulation sets the scale maximum. As demonstrated by Figure 17, microhalos are indeed already beginning to form by $z = 186$.

We are also interested in seeing the difference between the formation of a host halo in a universe with an EMDE and a standard radiation-dominated universe. Using the same location and radius of the host halo from the EMDE simulation, we collect snapshots of the formation of the analogous host halo in the standard radiation-dominated simulation. Figure 17 demonstrates that no substantial structure formation begins until redshift $z \approx 50$ in the absence of an EMDE.

The `Rockstar` halo catalog contains host halo information for each halo entry. An example of the tree structure used to store this information can be seen in Fig. 18. The data structure used is a one-dimensional array. For each halo, the number stored in this array corresponds to the halo ID of the parent. For host halos, a -1 is stored to indicate that the halo is indeed a host. In order to find all subhalos of a particular host halo, one must recursively traverse all the way down each branch of the tree. Namely, one must first find all of the first-level subhalos of the host. Then, for each subhalo, one finds all sub-subhalos. This continues until the bottom of the tree is reached. It is important to note that we employ a 100 particle minimum for `Rockstar` to identify structure. In particular, this rule applies to all levels of structure. The smallest size a subhalo can be is 100 particles. In Fig. 19, we use `MayaVi` to plot the `Rockstar`-identified locations of all substructure for a large host halo on top of the two-dimensional projection of the host halo density. The host halo is one of the largest from its EMDE simulation and demonstrates the substructure abundance that will contribute to the annihilation boost factors. Since the annihilation rate scales with density squared, the abundance of subhalos will cause a significant boost factor, to be computed in Section IV.

The Cartesian particle binning technique used in this subsection will be revisited in Subsection IV B, as it will also be used for numerical integration of J-factors. In the next subsection, we will utilize radial binning of particles to calculate density profiles. The density profile is quite sensitive to proper halo center identification by `Rockstar`. We demonstrate in the next subsection that we occasionally must re-calibrate the halo center to the most dense region in order to properly calculate density profiles.

E. Density Profiles

Another tool that we use to verify that our simulations agree with established literature is the density profile. In this subsection, we discuss the technique to numerically calculate density profiles of microhalos in our simulations. With this tool in place, we use the numerical density profile to fit a generalized NFW profile [19] of the form

$$\rho(r) = \frac{\rho_s}{(\frac{r}{R_s})^\gamma (1 + \frac{r}{R_s})^{3-\gamma}} \tag{53}$$

where R_s, ρ_s and γ are fit parameters. We will constrain γ to be positive, as a negative γ indicates a density which increases with radius. In the standard NFW profile, γ is set to unity. The NFW profile describes a nearly universal functional form for dark matter halo density profiles. We define the concentration of a halo $c = R_{200}/R_s$, where R_{200} is the halo radius from `Rockstar` and R_s is based on

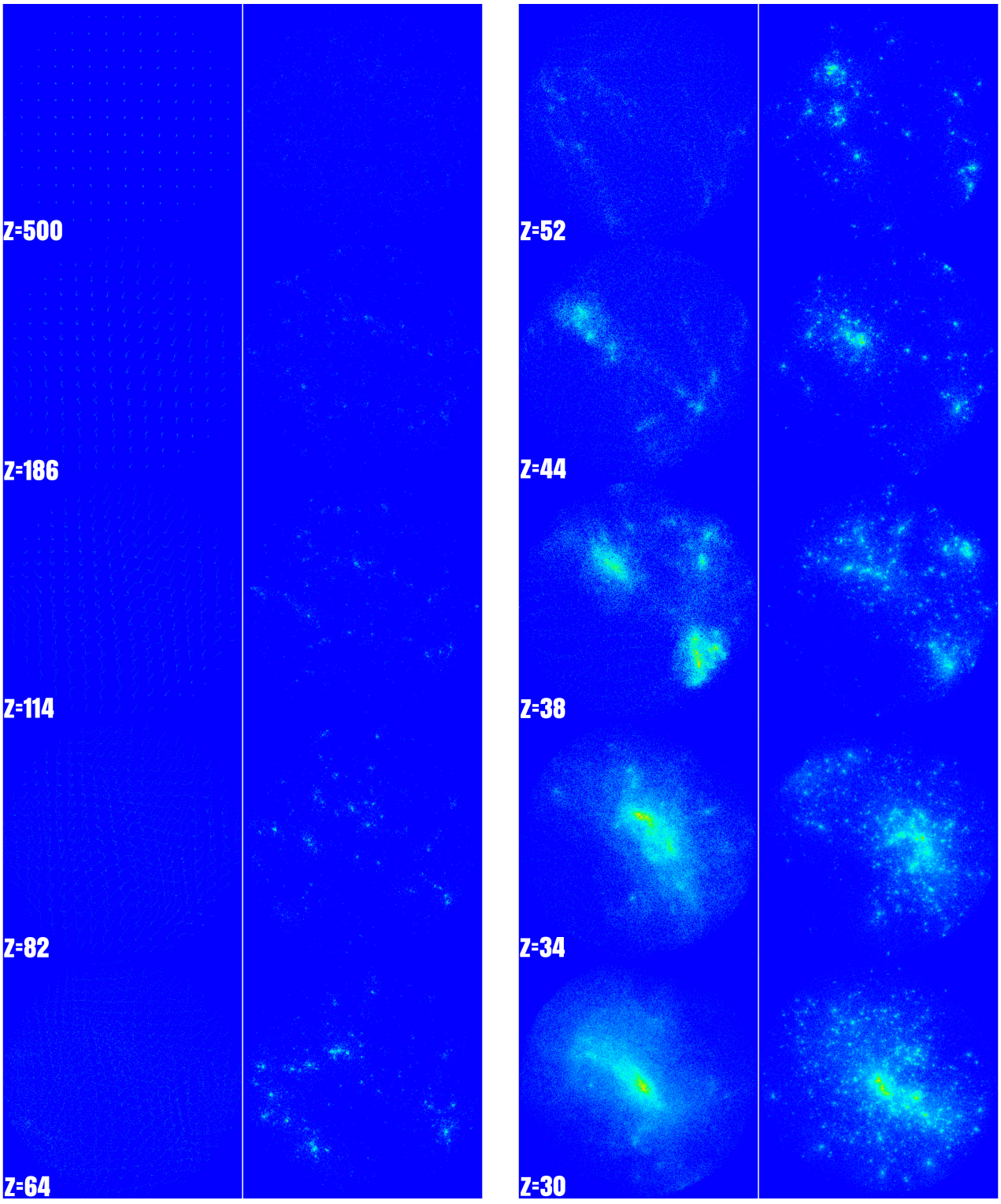

FIG. 17. A comparison of the evolution of a microhalo in a universe that undergoes an EMDE against the same microhalo in a standard radiation-dominated universe. In each of the two columns, the standard halo is on the left and the EMDE halo is on the right. The evolution begins at $z = 500$ in the top left and ends at $z = 30$ in the bottom right. Note the abundance of substructure in the EMDE halo. The same density color scale is maintained throughout all images.

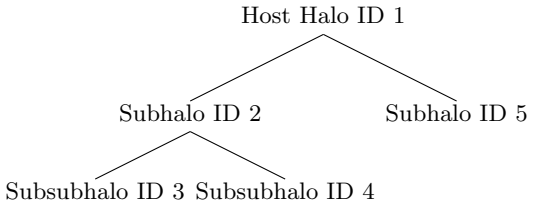

FIG. 18. Example diagram for substructure tree. In the tree array, index 1 would contain a -1, indicating that halo 1 is a host halo. Indices 2 and 5 would both contain a 1, indicating that halo 1 is the parent halo of halos 2 and 3. Indices 3 and 4 would both contain a 2, indicating that halo 2 is the parent halo of halos 3 and 4.

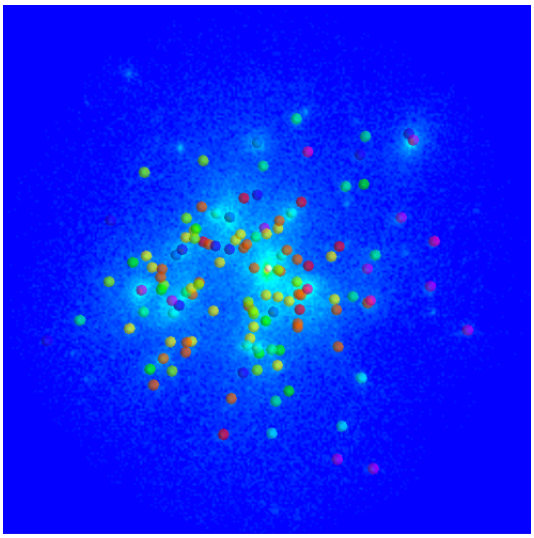

FIG. 19. Visual demonstration of substructure levels as identified by `Rockstar` for a large host halo from a 512^3 particle, $(30\ \mathrm{pc}/h)^3$ simulation of a universe that undergoes an EMDE. Levels of substructure closest to the host in the substructure tree are indicated by dark colors, whereas generations of substructure more distant from the host are indicated by bright colors.

the NFW profile fit. As a second NFW fit constraint, we will demand that $c \geq 1$, because a scale radius $R_s > R_{200}$ is unphysical.

The ρ_s of the NFW profile can be found by defining the integral of the profile out to R_{200} to be equal to M_{200}, thus:

$$M_{200} = \frac{4}{3}\pi R_{200}^3 f_\chi \rho_{200} = \int_0^{R_{200}} \frac{\rho_s}{\frac{r}{R_s}(1+\frac{r}{R_s})^2} 4\pi r^2 dr, \tag{54}$$

where $f_\chi = \rho_\chi/\rho_m$ is the dark matter fraction, $\rho_{200} = 200\rho_c$. After computing the integral and replacing radii in favor of the concentration, we find ρ_s in terms of the halo concentration:

$$\rho_s = f_\chi \frac{\rho_{200}}{3} \frac{c^3}{\ln(1+c) - c/(1+c)}. \tag{55}$$

Thus, the NFW profile can be defined in terms of the halo mass M_{200} and concentration c or in terms of the halo scale radius R_s and scale density ρ_s. We will now discuss difficulties in determining a mass-concentration relationship due to the resolution limit of our simulations.

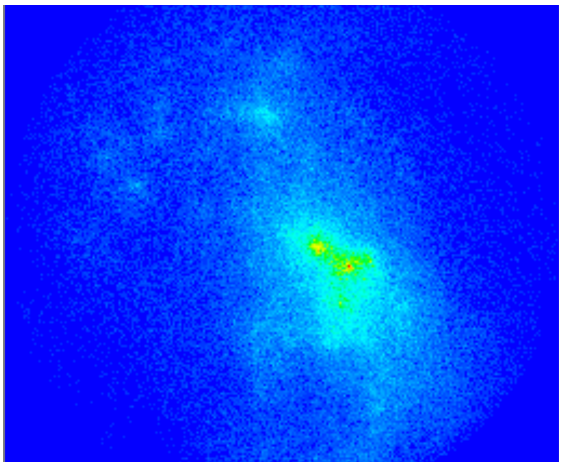

FIG. 20. Inaccurate centering of host halo by `Rockstar`. The center of the image is the location that Rockstar identified to be the host halo center whereas by eye the true center should be a bit below and to the right of the image center. Simulation specs: 512^3 particles, $(60\ \mathrm{pc}/h)^3$ box, standard radiation-dominated universe.

Modern cosmological simulations predict that the density profile of small microhalos just above the cut-off scale are rather cuspy, dropping off as $\rho \propto r^{-\gamma}$ near the halo's center, with $1.3 < \gamma < 1.5$ (Refs. [25, 26]). Larger microhalos often have $\gamma \approx 1$, which corresponds to the standard NFW profile [25, 26]. To fit an NFW profile, we must first accurately identify the central density peak of the halo. This central peak is defined to have $r = 0$. Unfortunately, `Rockstar` occasionally misidentifies the "center" of the halo, as seen in Figure 20. Our solution to this improper centering is as follows:

1. Begin by collecting halo particle data about the center and within the R_{200} radius as identified by `Rockstar`.
2. Bin the halo particles into a coarse-grained mesh.
3. Determine the bin with the largest number of particles.
4. Using the scale factor between the bin size and the comoving distance, find the location of the center of this bin with respect to the original halo center.
5. Collect particle data about this new center from the simulation snapshot.

We employ the method above for manually centering some halos in our calculation of density profiles. We note that this step is only necessary for density profile calculations. In our calculation of J-factors in Subsec. IV B, we will not manually center halos. Since the reference

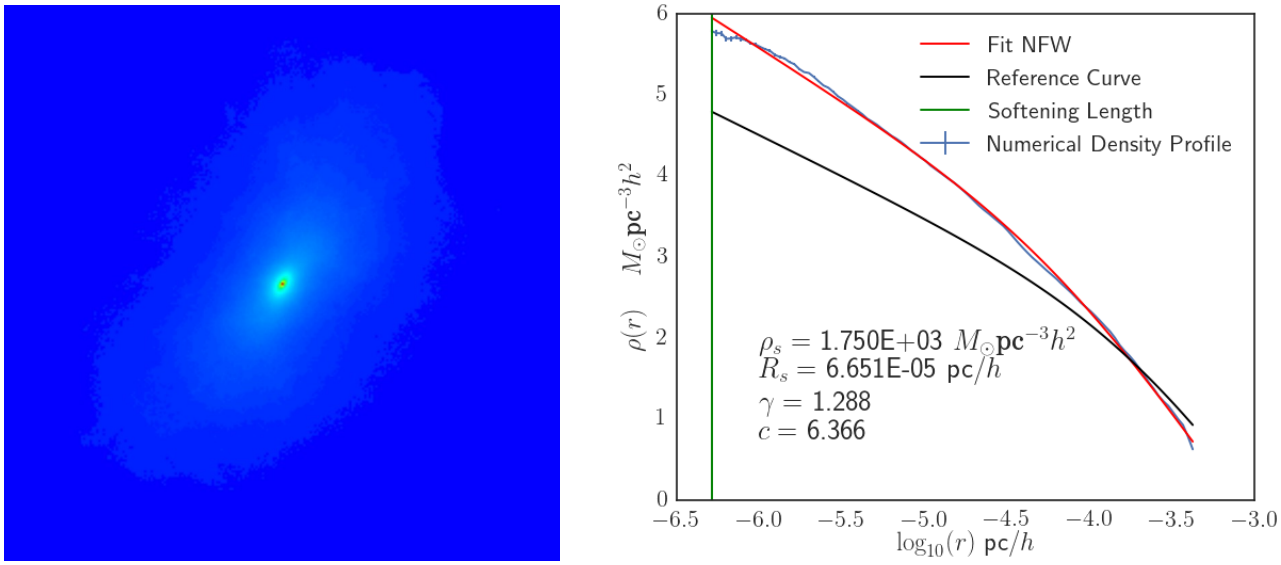

FIG. 21. On left: Visualization of high-resolution host halo from $(1\ \mathrm{pc}/h)^3$ box, 512^3 particle simulation. This is the largest halo in the simulation at $z = 100$ with $M_h = 7.9 \times 10^{-9}\ M_\odot/h$. On right: Density profile of the same halo. The numerical density profile is generated from halo particle data. Note that the Poisson error bars are extremely small due to the use of a high-resolution simulation. The fit NFW comes from a numerical fit of Eq. (53) using the SciPy `curve_fit` routine. The reference curve corresponds to an NFW profile with $c = 2.0$, $\gamma = 1$, and ρ_s according to Eq. (55).

integral, discussed in the next section, comes from a theoretically predicted NFW profile rather than a fit and the J-factor is just a numerical integral of density squared in Cartesian space, centering is not necessary for the calculation of boost factors.

In order to verify the halo formation in our simulations, we turn to the $(1\ \mathrm{pc}/h)^3$ box simulation. This simulation evolves until $z_f = 100$ and allows us to study the first generation of microhalos at a high resolution. After generating a halo catalog, we find the largest host halo in the simulation in order to calculate a high-resolution density profile and compare its NFW fit to predictions. To generate our numerical density profile, we take the halo particle data and translate their coordinates such that the origin corresponds to the halo center. We then create 100 bins that represent logarithmically-spaced three-dimensional annuli. The halo particles are then binned into these annuli based on their distance from the center. To calculate the density of each annulus $\rho(r_i)$, we have:

$$\rho(r_i) = N_{\mathrm{p,i}} M_p / \left(\frac{4}{3}\pi(r_i^3 - r_{i-1}^3)\right) \tag{56}$$

where $N_{\mathrm{p,i}}$ is the number of particles in a given annulus, M_p is the mass of a particle, and r_i is the radius of a given annulus. We define the innermost bin to have a radius corresponding to the softening length of the simulation. In this case, the softening length is defined as

$$r_{\mathrm{soft}} = \frac{1}{30}\frac{r_{\mathrm{box}}}{\sqrt[3]{N_{\mathrm{sim}}}} \tag{57}$$

where r_{box} is the comoving length of a side of the simulation box and N_{sim} is the total number of particles in the simulation. This corresponds roughly to 1/30 of the inter-particle spacing. We also demand that there be no less than 100 particles in the center annulus, and employ a routine which joins the innermost bins together until this condition is satisfied. The error on each bin is from Poisson noise, and thus for a bin with N particles, the error is $\sigma = \sqrt{N}$. Since we need substantially more than 100 particles to generate a good density profile, we are resolution limited to only the larger halos in our simulation for density profile calculations. An initial intention of this work was to produce a mass-concentration relation for microhalos analogous to the galaxy-mass halo mass-concentration relation of Ref. [27]. In order to successfully calculate this relationship, one would need considerably higher resolution such that even halos on the order of M_{cut} contain multiple thousands of particles.

The largest halo in the $(1\ \mathrm{pc}/h)^3$ box simulation has a mass of $7.9 \times 10^{-9}\ M_\odot/h$, an order of magnitude above the cut-off mass. In Figure 21, we compare the numerical density profile of this halo to its NFW fit. Note that the visualization shows a halo with a smooth, centrally-peaked density. In agreement with Refs. [25] and [26], we find that the small microhalos just above the cut-off mass do indeed have quite cuspy density profiles. In the case of the halo in Fig. 21, we find a $\gamma \approx 1.3$. Refs. [25] and [26] also demonstrate that microhalos that form in the absence of an EMDE typically have concentrations between 2 and 3 at a redshift of $z \sim 30$. Refs. [8–10] find that the concentration of halos scales with formation redshift, $c \propto (1 + z_f)$, and our preliminary results

indicate that the microhalos that are EMDE-generated do indeed have higher concentrations due to earlier formation. Our highest resolution halo has a concentration of $c = 6.4$ at $z = 100$, consistent with these expectations. In the absence of an EMDE, the earliest microhalos form no earlier than a redshift of 60, with concentrations between 2 and 3 at $z{\sim}30$. The concentration of a particular halo also increases as it evolves. Since R_s is expected to be roughly constant, and R_{200} scales as $(1+z)^{-1}$, we have that $c \propto (1+z)^{-1}$ [8, 9]. This means that we should expect even higher concentrations at our redshift of interest, $z_f = 30$.

We conduct the same analysis as above on the other top ten most massive halos from the $(1\ \mathrm{pc}/h)^3$ simulation. These halos fall in the mass range of just above $M_{\rm cut}$ to approximately $10M_{\rm cut}$. We find that for all of these halos, $1 < \gamma < 1.4$ and the concentrations fall in the range $2.5 < c < 12$, with the majority of the concentrations being above 4. This indicates that the EMDE-generated microhalos do indeed form earlier, resulting in increased halo concentrations at later times when compared to microhalos that form in a standard radiation-dominated universe. However, to complete this analysis we would need a more statistically complete sample of halos just above the cut-off mass. In order to do this, we would need to increase both the box size and the particle count. Unfortunately, this pushes outside our current range of computational resources. For now, we conclude our study of density profiles, moving on to calculating microhalo boost factors.

IV. BOOST FACTORS

In this section, we study the dark matter annihilation boost that is a result of the additional substructure formation due to an EMDE. In order to calculate the total boost factor as a function of galaxy host halo mass, we must first study the relationship between the boost factors of individual microhalos and their masses, denoted $B_s(M_{\rm mh})$. We denote the total boost $1+B$ to correspond to the dark matter annihilation boost in a galaxy-mass host halo due to its substructure, which includes microhalos, whereas B_s corresponds to the annihilation boost in individual microhalos due to their substructure. The microhalos of interest that will be used to numerically determine $B_s(M_{\rm mh})$ correspond to the host microhalos identified by `Rockstar` from our simulations. Recall that the boost factor for a microhalo is defined as

$$1 + B_s = \frac{J}{\int \overline{\rho}_\chi^2 4\pi r^2 dr} \tag{58}$$

where J represents the numerical integral of density squared over a particular microhalo and the denominator corresponds to a "reference integral" that we will discuss in Subsec. IV A. In order to calculate $B_s(M_{\rm mh})$, we must determine the boost factor for every microhalo in a given simulation. We discuss the resulting function in Subsec. IV C. Before this is possible, however, we must first determine the optimum manner to calculate the individual J-factors. We employ a simple three-dimensional Cartesian binning routine to determine J. Since each microhalo consists of a different number of particles from `GADGET-2` with a large range of R_{200} radii, this numerical integral must use an optimized resolution to accurately calculate the J-factor. This optimized resolution keeps contributions to the integral from Poisson noise to a minimum while still resolving individual contributions from microhalo substructure. In Subsec. IV B, we discuss the steps taken to determine the appropriate resolution as a function of microhalo particle count.

With our optimized bin function determined, we move on to calculating the boost factor of all microhalos in Subsec. IV C. With these boosts calculated, we employ the same mass binning technique used for the halo mass functions in Subsec. III B to bin the calculated boosts as a function of mass. The boost statistics in each bin are then used to determine a functional form for $B_s(M_{\rm mh})$ with remarkably small error bars. Kernel density estimation (KDE) is employed to generate a boost distribution for each mass bin, and samples are drawn from this distribution in an attempt to accurately reflect the number of microhalos in a given mass regime in a galaxy-mass host halo. We discuss the computational limits that prohibit drawing an equivalent number of samples to the $dN/d\ln M$ in each mass bin. Fortunately, we verify that convergence of each bin-averaged boost occurs at significantly lower sample sizes, mitigating the computational limits. We compare the $B_s(M_{\rm mh})$ calculated from each simulation box size to verify convergence of simulation results.

To determine the total boost factor of a galaxy-mass halo $1 + B$, we employ the analytical prediction from Ref. [11] with one key modification. The total fraction of dark matter bound into microhalos with $M < M_{\rm RH}$ at z_f is defined by Eq. (51). This factor plays significantly into the total boost factor prediction of Ref. [11]. Our technique for determining $1 + B$ will employ the same prediction except for the replacement of $f_{\rm tot}(z_f)$ with a boosted quantity $b_{\rm tot}(z_f)$ that functions as a weighted average of the microhalo boost factors with weighting from the differential bound fraction. This $b_{\rm tot}(z_f)$ is defined as

$$b_{\rm tot}(z_f) = \int_{\ln M_{\rm cut}}^{\ln M_{\rm RH}} [1 + B_s(M)] \frac{df}{d\ln M}\Big|_{z_f} d\ln M. \tag{59}$$

The calculation of this factor will be discussed in Subsec. IV D. With $b_{\rm tot}$ calculated, we introduce the full form of $1 + B$ from Ref. [11] and look at the mass dependence on the total boost. We finish off this section by discussing the observational implications of the calculated total boost factors.

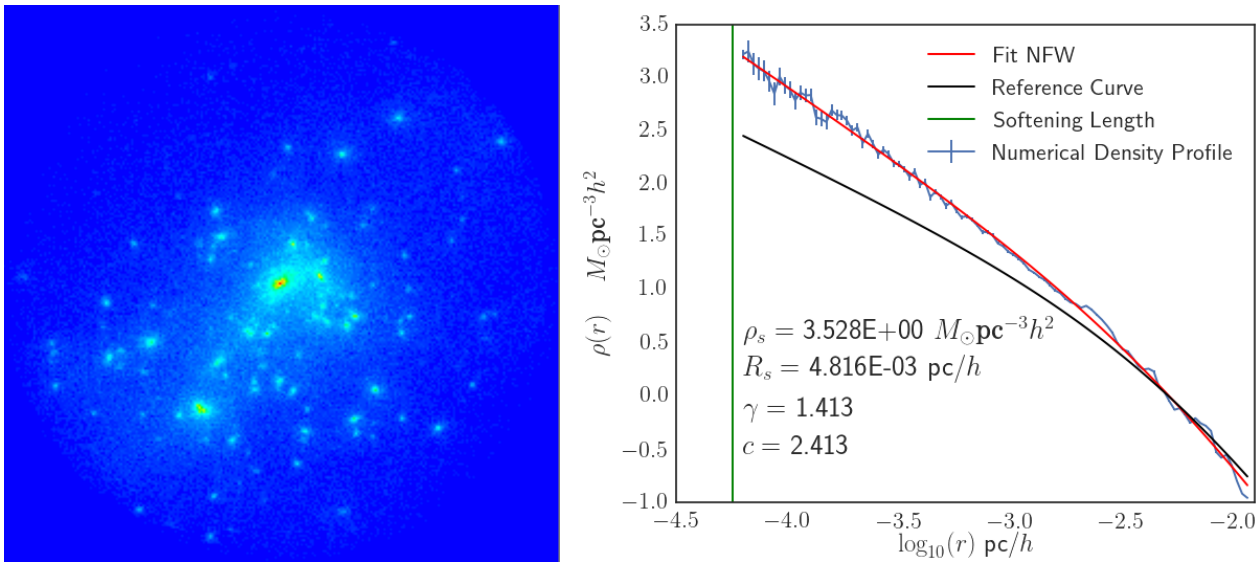

FIG. 22. On left: Visualization of substructure-dense host halo from $(30\ \text{pc}/h)^3$ box, 512^3 particle simulation. This halo has $M_h = 1.6 \times 10^{-6}\ M_\odot/h$ at $z_f = 30$, just below the reheat mass. On right: Density profile of the same halo. The same procedures are followed as in Fig. 21. Note the substructure bumps in the density profile at larger radii.

A. Reference Integrals

We now discuss the reference integral. Recall the definition of the boost factor from Eq. (1). The J-factor corresponds to the integral of the density squared across the volume of the halo of interest. This density is determined based on the particles from `GADGET-2`. The denominator of the boost factor is the reference integral. This integral is still a volume integral of density squared, but here the density is determined from a smooth, reference NFW profile. One practice that is often used is to remove all subhalo particle data from the host halo and fit an NFW profile to the smooth host halo profile in the absence of substructure. This smooth NFW is then used as the reference profile. However, for EMDE-generated host halos, a large fraction of the particles are bound into subhalos. By removing the substructure, we are left with very little to calculate an NFW profile from, and therefore this is an unreliable method of computing reference integrals. Instead, we will use a functional form for ρ_s and fix γ and c. In order to be consistent with the boost factor calculations of Ref. [11] in our comparisons, we will adopt a standard microhalo concentration of $c = 2$ for the reference profiles. This choice is motivated by Refs. [25, 26], which find that in the absence of an EMDE, simulated microhalos typically have a concentration of approximately 2 at $z_f = 30$.

By using a fixed concentration, the boost factor describes the boost in dark matter annihilation relative to a standard microhalo that forms in the absence of an EMDE. The NFW parameter R_s can be found directly with a fixed $c = 2$, such that $R_s = R_{200}/c$, with R_{200} from `Rockstar`. The preliminary analysis that suggests that an EMDE causes microhalos to form at higher redshifts, thus having higher concentrations at a given later time compared to a microhalo that forms later in the absence of an EMDE, also implies that the boost factors should be larger than if the EMDE halos still had concentrations of 2 to 3 at $z_f = 30$. This is because the power law transition occurs deeper into the halo for halos with higher concentrations, thus increasing the difference between the numerical density profile and the reference profile. This can be readily seen in Fig. 21, where the reference curve is substantially lower at most radii than the numerical density profile. We also set $\gamma = 1$ for all reference NFW profiles. Since many of the microhalos in the larger box simulations are substantially above the cut-off mass, $\gamma = 1$ is more appropriate than $\gamma > 1.3$. By $z_f = 30$, the larger halos will have undergone multiple mergers, and this is thought to soften out the density profile in standard scenarios [26]. With fixed $c = 2$, ρ_s can be calculated by Eq. (55). With these parameters as defined, we can calculate our reference curves. The reference curve in Fig. 21 demonstrates the corresponding reference NFW profile for our large halo from the $(1\ \text{pc}/h)^3$ simulation.

With the reference curve determined, we briefly study a large, substructure-dense microhalo from a $(30\ \text{pc}/h)^3$ simulation in Fig. 22. This halo is just below the reheat mass at $M = 1.6 \times 10^{-6}\ M_\odot/h$. Contrary to the expectation that $\gamma \approx 1$ for a large microhalo in the standard case [26], Fig. 22 suggests that an EMDE may result in microhalos with more cuspy profiles than their counterparts that form in a standard scenario. Clearly, this halo has formed by collecting abundant amounts of substructure throughout its evolution. Note that the numerical den-

sity profile has several "bumps" in it at larger radii that correspond to rather large subhalos. These bumps push the numerical density profile above the smooth fit NFW. When calculating J-factors, the square of the density is integrated. Therefore, these bumps in the density profile will become even more pronounced in the J-factor integration, ultimately leading to higher boost factors. In the next subsection, we discuss the necessary optimization in resolution such that substructure is resolved in the J-factor integral without artificially inflating the result due to Poisson noise.

B. J-Factor Resolution

Recall that the J-factor is the integral of density squared over the entire volume of a microhalo. Our method for calculating J is as follows. For each host microhalo identified by `Rockstar`, we collect the Cartesian coordinates of all particles within R_{200}. These particles are then binned into a three-dimensional mesh with n_j bins per dimension and total volume of $(2R_{200})^3$. We use the same number of bins in each dimension because dark matter halos are triaxial but roughly spherical. The focus of this subsection will be to determine $n_j(N_{\rm halo})$, with $N_{\rm halo}$ being the total number of particles in a host microhalo and all of its substructure. With these particles binned, we can then simply sum up the contributions from each individual bin. With M_p the mass of one particle and $V_{\rm bin} = (2R_{200})^3/n_j^3$, the density of bin ikl is $\rho_{ikl} = N_{{\rm p},ikl}M_p/V_{\rm bin}$. Therefore, the J-factor is thus:

$$J = \sum_{i=1}^{n_j}\sum_{k=1}^{n_j}\sum_{l=1}^{n_j}\Big(\frac{N_{{\rm p},ikl}M_p}{V_{\rm bin}}\Big)^2 V_{\rm bin} \tag{60}$$

with $V_{\rm bin}$ the volume element in the sum.

From this form, it is clear that it is imperative that substructure is adequately resolved in order to calculate J correctly. Were we to set $n_j = 1$ and just calculate the integral of the average density squared, none of the high-density substructure would be resolved to contribute to J. On the other hand, as $n_j \to \infty$, a point will be reached where every particle is assigned to its own bin and thus $N_{{\rm p},ikl} = 1$ or 0 and $J = N_{\rm halo}M_p^2/V_{\rm bin}$. Therefore, we expect that J will increase without bound as n_j increases, because $V_{\rm bin}$ decreases with increasing n_j. Figure 23 shows the J-factor for a particular halo as a function of n_j. Note that there appears to be an inflection point after which J begins to increase at an accelerated rate as $V_{\rm bin}$ continues to increase. This inflection point is present across a variety of halos. In fact, we could define our optimized n_j such that it is where the inflection point is located for a cubic fit polynomial to the $J - n_j$ plot. However, as we will show below, it is more reasonable to constrain n_j based on arguments related to error contributions rather than this inflection point.

The monotonic increase of J with increasing n_j demonstrates the need to optimize n_j based on the number of particles in the halo. We want to determine a resolution that accurately resolves substructure without Poisson noise domination. We test two separate constraints on n_j, both of which are motivated by minimizing the total contribution to J from Poisson noise. Firstly, we determine the analytical form of the Poisson noise and find the value of n_j that keeps the error below a certain fraction of the total J. In the case of our tests, we choose an upper bound of 10% Poisson error compared to J. We then employ a second constraint: we find the value of n_j such that greater than 80% of J comes from nonempty bins with greater than 10 particles. The more strict of these two constraints sets our upper bound on n_j.

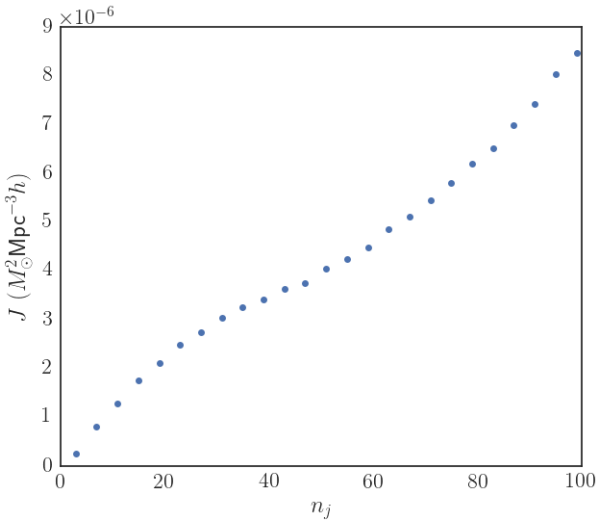

FIG. 23. J vs. n_j for an approximately 10,000 particle halo from a $(30\ \mathrm{pc}/h)^3$ EMDE simulation. Note the inflection point at $n_j \approx 40$, whereas Eq. (65) uses an $n_j = 25$. A fit of the post-inflection point data up to $n_j = 200$ shows that $J \propto n_j^{1.8}$, indicating that the decreasing bin size is not yet the dominant reason for increasing J. In the case of high n_j, we expect $J \propto n_j^3$.

The Poisson error on a bin with N particles inside of it is $\sigma = \sqrt{N}$. To study how the Poisson error contributes to the J-factor, we consider the case of a halo with an average bin occupation of $N = N_{\rm halo}/n_j^3$. If the halo had a uniform density in all bins, the J factor would be $J = n_j^3 M_p^2 N^2/V_{\rm bin}$. However, with a standard deviation from Poisson noise, we can write the bin occupation as $N \pm \sqrt{N}$. Consider J to be the sum over all of these bins with random Poisson noise:

$$\begin{aligned} J &= \sum_{i,k,l}^{n_j} V_{\rm bin} M_p^2 \Big(\frac{N_{{\rm p},ikl}}{V_{\rm bin}} \pm \frac{\sqrt{N_{{\rm p},ikl}}}{V_{\rm bin}}\Big)^2 \\ &= \sum_{i,k,l}^{n_j} V_{\rm bin} M_p^2 \Big[\frac{N_{{\rm p},ikl}^2}{V_{\rm bin}^2} \pm \frac{2N_{{\rm p},ikl}\sqrt{N_{{\rm p},ikl}}}{V_{\rm bin}^2} + \frac{N_{{\rm p},ikl}}{V_{\rm bin}^2}\Big] \end{aligned} \tag{61}$$

and by averaging across all n_j^3 bins, the $\pm\frac{2N_{\mathrm{p},ikl}\sqrt{N_{\mathrm{p},ikl}}}{V_{\mathrm{bin}}^2}$ term vanishes so that

$$\langle J\rangle = \frac{M_p^2}{V_{\mathrm{bin}}}\sum_{i,k,l}^{n_j}\Big(N_{\mathrm{p},ikl}^2 + N_{\mathrm{p},ikl}\Big) \approx \frac{M_p^2 n_j^3}{V_{\mathrm{bin}}}\Big(N^2+N\Big). \tag{62}$$

This shows that the error in the calculation of the J factor can be found approximately by calculating the integral of the density whereas J is the integral of the density squared. In practice, this means that to determine the relative error fraction we simply compare the sum across all bins of the particle counts in each bin to the sum across all bins of the square of the particle counts in each bin.

In this calculation, we only consider bins with $N_{\mathrm{p},ikl} \geq 10$, because Poisson error $\sqrt{N}$ does not apply well in the limit of small counts. Therefore, we only compute the sums of density and density squared across bins with $N_{\mathrm{p},ikl} \geq 10$:

$$f_e = \frac{\sum_{i,k,l}^{n_j} N_{\mathrm{p},ikl}}{\sum_{i,k,l}^{n_j} N_{\mathrm{p},ikl}^2}\Big|_{N_{\mathrm{p},ikl}\geq 10} \leq 0.1\,. \tag{63}$$

Clearly, f_e increases with n_j. Our first constraint demands that n_j be below the point that makes $f_e = 0.1$.

We now employ a second constraint and then determine which of the two is more conservative. We note that by choosing the more conservative, lower n_j, we can only under-approximate the J-factor. Because of these under-approximations, our results for global $1+B$ in Subsec. IV D can be treated as lower bounds. In our second constraint, we demand that the total contribution to J from cells with $N_{\mathrm{p},ikl} \geq 10$ make up at least 80% of the total J. For this, we calculate:

$$f_{N\geq 10} = \frac{\sum_{i,k,l}^{n_j} N_{\mathrm{p},ikl}^2|_{N_{\mathrm{p},ikl}\geq 10}}{\sum_{i,k,l}^{n_j} N_{\mathrm{p},ikl}^2} \geq 0.8. \tag{64}$$

Clearly, $f_{N\geq 10}$ will decrease as n_j increases.

As a test to determine which constraint we will want to look at across a broad range of halos, we test several halos from the $(30\ \mathrm{pc}/h)^3$ EMDE simulation. These tests are conducted as follows: for each halo, the quantities $f_{N\geq 10}$ and f_e are calculated for an array of n_j values. We then find the the highest value of n_j such that neither of the constraints is violated. The second constraint, as given by Eq. (64), is much more conservative. For example, a 719 particle halo has $n_j = 23$ when $f_{N\geq 10} \approx 0.8$. However, $f_e \approx 0.03$ at this n_j. Similar results are found for a wide variety of halo masses up to nearly 200,000 particles. In particular, regardless of the n_j such that $f_{N\geq 10} \approx 0.8$, it is always the case that $f_e \lesssim 0.05$. For this reason, we choose the more conservative constraint that $f_{N\geq 10} \geq 0.8$. Using this constraint, we calculate the maximum n_j for several thousand halos from the simulation across a spread of mass regimes. We note that since a 1024^3 particle EMDE simulation contains approximately 100,000 host halos, computing the optimum n_j by repeatedly calculating J for different n_j would be computationally intractable to be done across the entire dataset. In Fig 24, we plot the numerically calculated maximum n_j above the given constraint for these halos. We then fit a cubic to the data in log-log space to define a relationship between n_j and N_{halo}. This relationship will be employed in the next subsection to calculate the J factors and ultimately $B_s(M_{\mathrm{mh}})$:

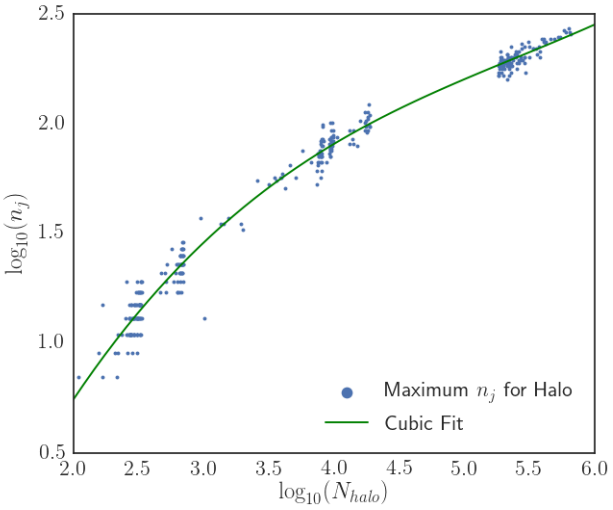

FIG. 24. Maximum n_j that does not violate the constraint of Eq. (64) for `GADGET-2` halos across full range of particle counts. The cubic fit function is described by Eq. (65).

$$\begin{aligned}\log_{10}(n_j) =& 0.01836\log_{10}(N_{\mathrm{halo}})^3 - 0.298091\log_{10}(N_{\mathrm{halo}})^2 \\ &+ 1.856971\log_{10}(N_{\mathrm{halo}}) - 1.925952\,.\end{aligned} \tag{65}$$

With our functional form for $n_j(N_{\mathrm{halo}})$ determined, we want to study the effect on J from averaging out the central density cusp of the halo. Recall the NFW profile from Eq. (53). As $r \to 0$, $\delta \to \infty$. It is likely that the N-body simulation is not able to fully capture the maximum density of the cusp at the center. Even if there were enough particles to capture a good halo cusp, our numerical integral of J smooths out the central peak of the density profile. We now calculate the contribution to J from the central bin, where $r = 0$ is contained, assuming two different cases. In the first case, we assume J can indeed resolve the NFW density ρ exactly. In the second case, we calculate the contribution to J with the mean density of the bin $\bar{\rho}$, calling this value $\bar{J}$.

Suppose a bin length R_p. For $r \ll R_s$, $\rho_{\mathrm{nfw}}(r) \approx \frac{\rho_s}{r/R_s} = \rho_s R_s/r \propto r^{-1}$. Since $J = \int_0^{R_s} 4\pi r^2 \rho_{\mathrm{nfw}}^2(r)dr$, the full J factor contribution from the central bin is

$$J = 4\pi\rho_s^2 R_s^2 R_p. \tag{66}$$

In order to calculate the mean density of the central bin, we need to determine the total mass enclosed within the

central bin using $\rho_{\rm nfw}$:

$$M = \int \rho dV = \int_0^{R_p} 4\pi r^2 \frac{\rho_s R_s}{r} dr = 2\pi\rho_s R_s R_p^2. \quad (67)$$

With this, the mean density of the central pixel is $\bar{\rho} = M/V_p = \frac{3}{2}\rho_s R_s/R_p$. With this mean density, the J factor contribution from the central bin is

$$\bar{J} = \int_0^{R_p} 4\pi r^2 \bar{\rho}^2 dr = \int_0^{R_p} 4\pi r^2 \Big(\frac{3\rho_s R_s}{2R_p}\Big)^2 dr = 3\pi\rho_s^2 R_s^2 R_p \quad (68)$$

Interestingly, the value of R_p drops out and we find that $J/\bar{J} = 4/3$. Therefore, since we calculate the central bin using $\bar{\rho}$ in our numerical integral of J, we are at most missing a factor of 1/3 of the central pixel's contribution to the total J. Provided that the resolution is high enough for the central bin to contribute a relatively small amount, such as less than 5% of the total, the numerical approximation of the central bin will not make a significant difference on our results. For low n_j, the central bin contributes a significant portion of the total J-factor. For this reason, we explicitly use only odd n_j so as to not split the central bin into 8 smaller bins, thus reducing the contribution from the density squared of the central peak and decreasing the J-factor. When calculating J-factors, we employ Eq. (65) such that n_j is rounded down to the nearest **odd** integer. We now have all the necessary pieces to calculate $B_s(M_{\rm mh})$. Using reference integrals from Subsec. III E and the J-factor calculation technique and resolution function from this subsection, we now proceed to calculate the substructure boost-mass relationship in the following subsection.

C. Substructure Boost-Mass Relationship $B_s(M_{\rm mh})$

With all the necessary tools in place, we proceed to calculate the boost factor of every host microhalo identified in our simulations. The process is fairly simple. For each host, we numerically calculate J using the procedure in Subsec. IV B. We then calculate the reference integral defined in Subsec. III E based on the halo parameters. Using Eq. (1), we divide J by the reference integral to get $1 + B_s$. This process is iterated over all host halos in the `Rockstar` halo catalogs for each of the EMDE and standard simulations. The information stored is B_s and $M_{\rm mh}$ for each microhalo. To begin our analysis, we study the 30 $({\rm pc}/h)^3$ EMDE simulation in Fig. 25. In this figure, there are approximately 100,000 host halos, each of which have a boost factor B_s calculated. Note that we are plotting B_s rather than $1 + B_s$. Therefore, on the logarithmic scale, the lower B_s correspond to halos that are nearly substructure-less whose J agrees very closely with the reference integral.

In order to calculate statistics on this data and construct a function $B_s(M_{\rm mh})$, we bin the halos according to the same mass bins that were used for the mass functions from Subsec. III B. Within these mass bins, we can study the distributions of B_s. We demonstrate these distributions for several mass bins in Fig. 25. For each bin, we calculate the median and quartiles. As demonstrated by the median and quartile curves in the figure, the data is fairly tight with little room between the inner quartiles.

This $B_s(M_{\rm mh})$ function describes the boost statistics from the simulation. In these calculations, we are limited to the number of halo samples that are present in our `Rockstar` catalogs. To determine the total boost in a galaxy-mass host halo today, we need to know the total number of microhalos that have survived in the host halo as a function of mass. We can then use these microhalo number statistics alongside our $B_s(M_{\rm mh})$ distributions in each mass bin to calculate representative means and uncertainties of the microhalo boost in each mass bin. The number density of microhalos within a halo is determined by the differential bound fraction at z_f from Eq. (50):

$$\frac{dn_{\rm mh}}{d\ln M_f} = s(r)\frac{\rho_{\rm halo}(r)}{M_f}\frac{df}{d\ln M_f}\Big|_{z=z_f} \quad (69)$$

where M_f is the mass of the microhalo at high redshift, namely $z_f = 30$. Here, $\rho_{\rm halo}(r)$ is the spherically-averaged present-day density of the host halo as a function of the distance from the center and $s(r)$ is the "survival fraction" as a function of distance from the center, namely the fraction of microhalos present at z_f that survive to the present day [11]. To transform from microhalo number density to total microhalo counts per mass bin, we simply integrate Eq. (69) over the volume of the halo $V_{\rm halo}$ while holding $s(r) = 1$. Therefore, the total number of halos in the host halo per mass bin is:

$$\frac{dN_{\rm mh}}{d\ln M_f} = \frac{M_{\rm halo}}{M_f}\frac{df}{d\ln M_f}\Big|_{z=z_f}. \quad (70)$$

We need to understand the distribution of boost factors within each mass bin in order to draw $\frac{dN_{\rm mh}}{d\ln M_f}$ samples from this distribution and calculate the statistics on the boost-mass relationship of all microhalos within a galaxy-mass host. We would like to fit a distribution function to the boost distributions within each mass bin. However, as indicated by Fig. 25, the distribution shape changes with the mass bin. Rather than fit a Gaussian or Poisson distribution, we employ a kernel density estimation (KDE) from the `scikit-learn` module for Python [28]. This is known as a nonparametric distribution fitting technique. We use a Gaussian kernel and optimize the bandwidth with 2-fold cross-validation. Ultimately, the KDE routine creates a distribution for each mass bin that agrees well with the data, as seen by the KDE curves in Fig. 25. Assuming that the boost distributions from our numerical calculations of `GADGET-2` halos are representative of true microhalo populations within each mass bin of interest for a galaxy-mass host halo, we can then sample from the corresponding KDE distributions a total of $\frac{dN_{\rm mh}}{d\ln M_f}$ times per bin.

At this point, we run into a computational challenge: for each of the approximately 30 mass bins, for a $10^6\ M_\odot$

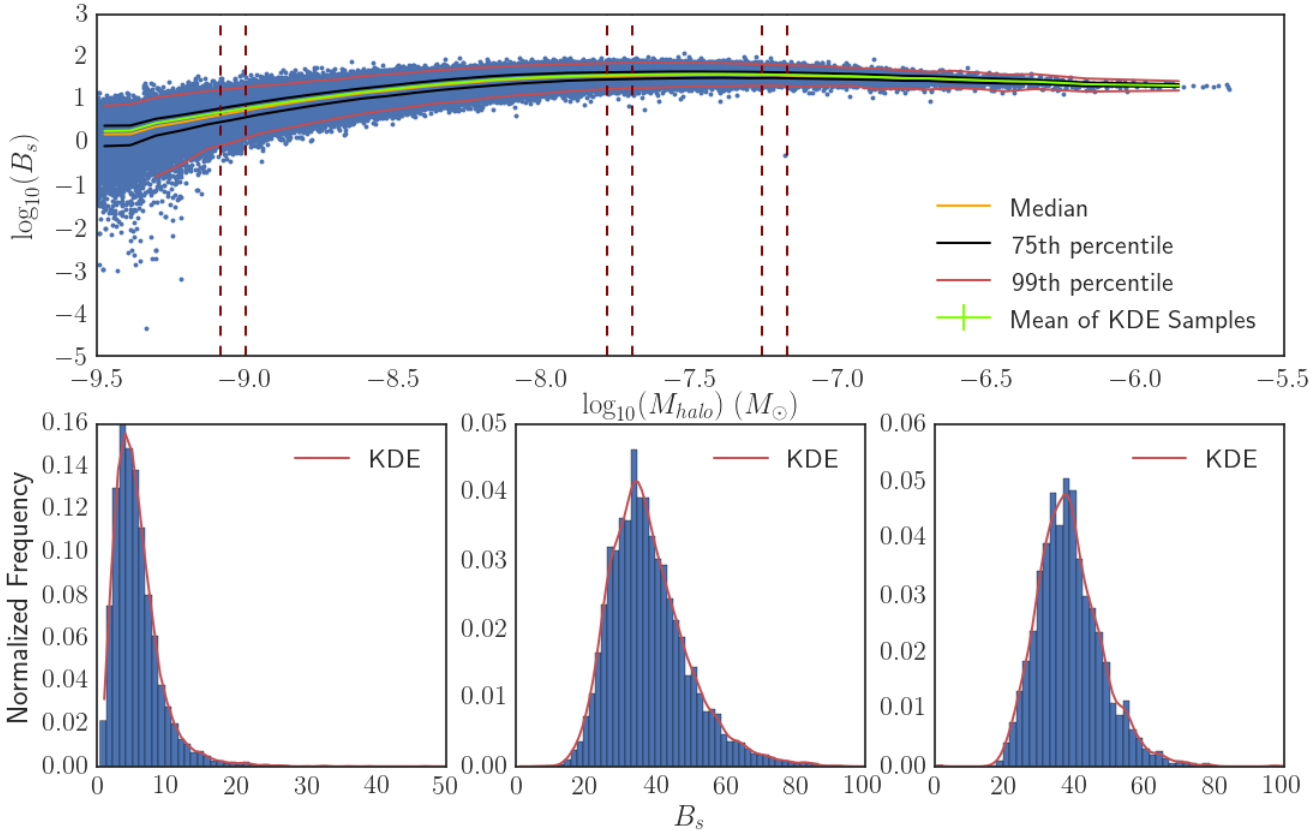

FIG. 25. Top: Calculated boost-mass relationship for the microhalos from the $(30\ \mathrm{pc}/h)^3$ EMDE simulation. The median and quartile lines illustrate a tight relationship with little scatter. The mean is determined by sampling from the KDE of each mass bin. Ideally, we would make $dN/d\ln M_f$ samples per mass bin, but the number converges much earlier. The error bars on the mean B_s in each bin across multiple trials are negligible, as explained in the text. Bottom: Each of the three distributions corresponds to the boosts within a particular mass bin, indicated by the vertical dashed lines in the upper plot, from left to right. The KDEs were calculated using 2-fold cross validation to determine the optimum bandwidth.

dSph galaxy, $\frac{dN_{\rm mh}}{d\ln M_f}$ is on the order of 10^{10} to 10^{12}. We need to draw this many samples from the KDE boost distribution for each bin. This is computationally intractable, but also unnecessary. Since we are only interested in the mean and standard deviation of the boost in each mass bin from this large number of samples, we can study the convergence of the mean as a function of samples from the distribution. In Fig. 26, we look at the convergence of B_s in a particular mass bin as a function of the number of samples. Clearly, the average value of B_s has converged to the second decimal place by 10^6 samples drawn from the KDE distribution. Therefore, we do not need to sample $\frac{dN_{\rm mh}}{d\ln M_f}$ boosts per bin. We select $N_{\rm kde} = 10^6$ as the number of samples taken from the KDE.

We now have an average boost for each mass bin using the above procedure. In the next subsection we use these averages to define our $B_s(M_{\rm mh})$ in the calculation of $b_{\rm tot}(z_f)$. To understand the error on $b_{\rm tot}(z_f)$, we need to calculate it for multiple trials. In particular, one trial consists of sampling $N_{\rm kde}$ samples from each mass bin to calculate an average boost, defining $B_s(M_{\rm mh})$, and then calculating $b_{\rm tot}(z_f)$. As a test, we iterate the first half of this procedure $N_{\rm trials} = 10^4$ times to look at the distribution of average boosts for the same mass bin that we used to test convergence. Fig. 26 demonstrates that for 10^4 trials, each of which has its own calculated average boost for the mass bin from 10^6 KDE samples, the standard deviation of average B_s values is around $\sigma = 0.01$ with means ranging from 1 to upwards of 20 depending on the mass bin. In Fig. 25, we plot the mean B_s in each mass bin across $N_{\rm trials}$, each of which consist of $N_{\rm kde}$ samples. The standard deviations of all of the B_s averages are shown as error bars on the plot that are significantly smaller than the width of the mean line.

We conclude the error analysis with an important note: as $N_{\rm kde}$ increases towards $\frac{dN_{\rm mh}}{d\ln M_f}$, the average B_s over $N_{\rm trials}$ distinct trials converges. Our conclusion is that when calculating B_s in a mass bin for a galaxy-mass host halo, there is no significant scatter in this boost when compared to other host halos. This is ultimately because the boost distributions in each bin from the halos in our `Rockstar` catalog have tight inner quartiles, and if we were to sample $\frac{dN_{\rm mh}}{d\ln M_f}$ halos from each bin, the

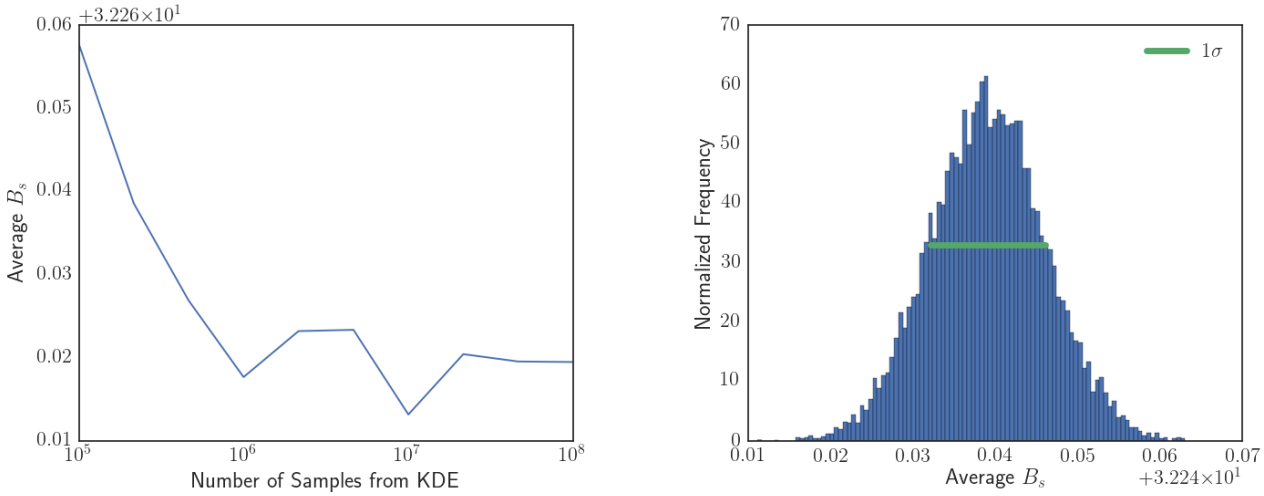

FIG. 26. On left: Demonstration of convergence of the average B_s in a mass bin centered at $\log_{10}(M/M_\odot) = -6.8$. By 10^6 samples from the KDE, the average has converged to the second decimal place. On right: With $N_{\rm kde} = 10^6$, we calculate the average B_s in the same mass bin a total of $N_{\rm trials} = 10^4$ times and look at the distribution of the averages. The error bar on this distribution is approximately $\sigma = 0.01$. These different values of average B_s will be used to calculate $b_{\rm tot}$ in the next subsection.

average for this set of samples is going to consistently lie almost exactly at the peak of the KDE distribution. Across multiple trials of calculating the average B_s in a particular mass bin, we find negligible variance. However, this does not imply that the calculation of the $B_s(M_{mh})$ relationship and ultimately the total galaxy-mass boost factor has no uncertainty. Rather, the uncertainty is primarily attributed to our selection of a resolution n_j for the calculation of each J-factor that ultimately made the mass bin distributions that we are sampling from. This uncertainty is difficult to quantify, so we continue forward without directly considering the error from B_s in our later calculations. An analysis of the error due to J-factor resolutions is left to future work.

Thus far, all of our analysis of B_s has been conducted only with the $(30\ {\rm pc}/h)^3$ EMDE simulation. We would like to check for consistency between the various box sizes and compare the overall $B_s(M_{\rm mh})$ functions between the EMDE and standard simulations. We conduct all of the same analysis as described above across all of the simulations and report the results in Fig. 27. The key results are as follows. We find that the average boosts for all mass bins are larger for smaller simulation box sizes. This is expected, as the smaller box size simulations have smaller particle masses. More high-density substructure can be resolved for any given host microhalo as particle mass decreases, and thus the J-factor will increase as more substructure is integrated over. Since the minimum halo mass in our $(30\ {\rm pc}/h)^3$ box is below the free-streaming cut-off mass, it is likely that this simulation has captured nearly all of the substructure boost. However, further convergence testing should be considered, as a higher resolution simulation with lower particle mass may uncover additional boost due to larger n_j resolving more substructure. We expect that as the resolution increases, the average $B_s(M_{\rm mh})$ in each mass bin should converge. Because the $(30\ {\rm pc}/h)^3$ box is the smallest simulation and has the highest resolution, we will study the results of only this simulation in the following subsection when calculating the total galaxy-mass boost factor. Fortunately, the $(30\ {\rm pc}/h)^3$ box has a fairly high resolution while also still allowing for halo formation up to the reheat mass scale, allowing us to probe the full range of microhalo boost factors for microhalos between $M_{\rm cut}$ and $M_{\rm RH}$. Since the boosts in each mass bin increase as we increase our resolution, we expect that all results in the following subsection correspond to lower bounds.

Fig. 27 also shows boost factors of the microhalos from the standard simulations. Due to the use of a reference integral based on analytic predictions with a smooth NFW profile and the fact that there is still some substructure in the absence of an EMDE, we get nonzero boosts in the standard simulation as well. This shows that there is still some substructure in larger host halos even in the absence of an EMDE, with B_s leveling out at a value around 3 for high mass microhalos. With our $B_s(M_{\rm mh})$ relationship completed, we move onwards to the next subsection, where we calculate the galaxy-mass boost factor $1 + B$.

D. Total Boost $1 + B$

Up to this point, all of our boost calculations have been made for microhalos at a fairly high redshift $z_f = 30$. The cosmological simulations help provide a better understanding of the fraction of microhalos that survive from their formation redshift at $z \approx 100-200$ up until the

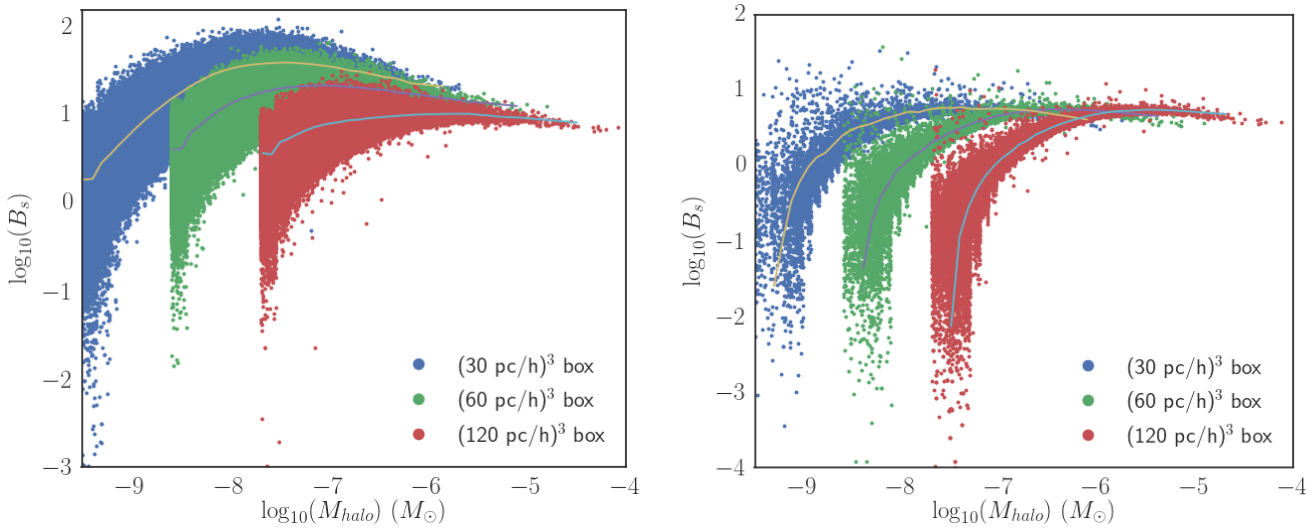

FIG. 27. On left: Boost-mass relationship for all microhalos from `Rockstar` catalogs in the 30, 60, and 120 $(\mathrm{pc}/h)^3$ box EMDE simulations. The curves correspond to the means from KDE samples for each respective simulation. The inconsistencies between the simulation averages is due to additional substructure resolution in smaller box sizes. On right: Boost-mass relationship for all microhalos in the corresponding standard simulations and their associated averages from KDE samples.

end of our simulation z_f. The abundance of primordial microhalos as substructure in sub-reheat mass hosts at z_f demonstrates a boost B_s on the order of 10 for the largest of microhalos. We would like to use all of this information to determine the total boost of a galaxy-mass host halo today ($z = 0$). We follow the analytical prediction made by Ref. [11], which calculates the total boost factor of a host halo today by splitting the J-factor into three separate contributions.

The first contribution to the total J-factor is from the microhalos that have survived up to today. The primary mechanism by which microhalos are destroyed is tidal stripping. Ref. [29] demonstrates that a subhalo with an NFW profile scale radius r_s is completely destroyed if its tidal radius r_t is less than twice its scale radius. We now adopt the notation that r corresponds to a microhalo-associated radius while R corresponds to a host-associated radius. Ref. [11] finds that for all host halo masses, $r_t/r_s > 2$ for all microhalos at position within the host halo $R > R_{\rm min} \equiv \sqrt{R_s/(100\mathrm{kpc})}$ kpc, where R_s is the NFW scale radius of the host.

In the analytic predictions, Ref. [11] calculates the J-factor of an individual microhalo $J_{\rm cl}$ by truncating the density profile at $r = r_s$ to account for partial tidal stripping and neglects the negligible reduction due to a constant density core:

$$J_{\rm cl}(M,z) = [1+B_s(M)]\frac{7}{6}\pi\rho_s^2 r_s^3 = f_\chi^2 \frac{M}{3}\rho_{200}(z)c(z,z_{\rm f})^3 \frac{7[1+B_s(M)]}{24[\ln(1+c)-c/(1+c)]^2}, \quad (71)$$

where z_f is the formation redshift for a microhalo with mass $M \approx M_{200}(z)$. Recall that $\rho_{200}(z) = 200\rho_c(z)$, where $\rho_c(z)$ is the critical density at redshift z. Also recall that the concentration $c(z, z_f) = r_{200}/r_s$, which we set equal to 2 for all microhalos because Refs. [25, 26] find that simulated microhalos typically have a concentration of approximately 2 at $z = 30$ in the absence of an EMDE. Lastly, we incorporate the $[1 + B_s(M)]$ factor to account for the substructure boost in individual microhalos found from our simulations. The possible reduction in ρ_s due to stripping is neglected because we assume that the microhalos form with a high enough central density to remain tightly bound once their outer layers are tidally stripped, rather than begin to relax to a lower ρ_s.

The individual microhalo J-factors will be evaluated at the same redshift as the microhalo mass function. Our simulations end at $z_f = 30$, and this is the redshift that the mass function is evaluated. Since the concentration $c \propto (1+z_f)$, a halo that forms at a higher redshift should have a higher concentration, thus increasing $J_{\rm cl}$. In Ref. [11], microhalos are treated as if they formed shortly before the calculation of the bound matter fraction $f_{\rm tot}(z_f)$, thus providing a lower bound on the boost factor. Since the bound matter fraction increases monotonically with time, as shown in Fig. 16, choosing a large value for z_f ignores contributions to the total microhalo J-factor from later-forming microhalos. However, choosing a low z_f and continuing to use $c = 2$ for the microhalos neglects the fact that many of the microhalos formed earlier and have higher concentrations and increased substructure, both of which contribute to the J-factor. The numerical simulations provide information about the halo populations at $z_f = 30$, which allows us to incorporate the contributions from both later-forming microhalos and substructure that becomes present in earlier-forming microhalos into the total microhalo J-factor.

The total contribution to the host halo J-factor from microhalos is the sum over all the individual microhalo $J_{\rm cl}$ factors within the host. This is found by integrating the host halo density with the radius-dependent survival rate $s(r)$ multiplied by the total fraction bound into microhalos to get the total mass of microhalos in the host. This puts a lower bound on $J_{\rm micro}$ to be:

$$J_{\rm micro} \gtrsim \frac{(7/72)\rho_{200}(z_f)c^3 f_\chi^2}{[\ln(1+c)-c/(1+c)]^2}\int_0^R s(r')\rho_{\rm halo}(r')\mathrm{d}^3r' \times \int_0^{\ln M_{\rm RH}}[1+B_s(M)]\frac{df}{d\ln M}\Big|_{z_f} d\ln M. \tag{72}$$

The reference curves used to calculate $B_s(M)$ demands that we take $c = 2$ for the microhalos at z_f. We note that $\rho_{200}(z_f) \propto (1+z_f)^3$. Thus, in an analytical prediction of the total boost, $J_{\rm micro}$ dramatically increases for earlier nonzero $f_{\rm tot}(z_f)$. In this work, we do not need to optimize for z_f due to uncertainty in halo formation time and microhalo evolution. By incorporating $1 + B_s(M_{mh})$ into our calculation, we are accounting for additional substructure formation for host halos below the reheat mass that will increase the overall subhalo boosts in the galaxy-mass host halo. Doing this, we now include a differential bound fraction-averaged boost parameter $b_{\rm tot}(z_f)$ as defined in Eq. (59) that is present in our calculation of $J_{\rm micro}$ in Eq. (72). This quantity is calculated by summing

$$b_{\rm tot}(z_f) = \sum_i [1+B_s(M_i)]\frac{df}{d\ln M_i}\Delta(\ln M_i) \tag{73}$$

where the sum runs over all mass bins centered at $\ln M_i$ with bin widths $\Delta(\ln M_i)$. For the $(30\ \mathrm{pc}/h)^3$ EMDE simulation, we find a $b_{\rm tot}(z_f) = 23.7$. We compare this to the calculation for the $(30\ \mathrm{pc}/h)^3$ standard simulation as a control, finding a $b_{\rm tot}(z_f) = 0.14$.

As discussed above, the microhalos outside of $R_{\rm min}$ are expected to survive destruction due to tidal stripping. Therefore, the microhalo survival rate $s(r')$ is fixed to 0 inside $R_{\rm min}$ and 1 outside $R_{\rm min}$. With all this accounted for, Eq. (72) simplifies to

$$J_{\rm micro} \gtrsim 4 f_\chi^2 \rho_{200}(z_f) b_{\rm tot}(z_f) M_{\rm halo}(r > R_{\rm min}). \tag{74}$$

with $M_{\rm halo}(r > R_{\rm min})$ the mass of the host halo contained outside of $R_{\rm min}$, found by integrating an NFW profile for the host from $R_{\rm min}$ to R_{200}. For the NFW parameters, ρ_s is found from Eq. (55) according to the mass-concentration relation from Ref. [27] and R_s is found with $R_s = R_{200}/c_h$.

The dominant contribution to the total boost factor is $J_{\rm micro}$. However, we must also consider the contributions from the host halo and its subhalos with $M > M_{\rm RH}$. We introduce $f_s(r)$, the fraction of dark matter that is **not** contained in microhalos today as a function of radius from the center of the host halo. This is different from $f_{\rm tot}(z_f)$, which describes the total fraction of dark matter that is bound into microhalos as a function of redshift. Clearly, we have that $f_s(r < R_{\rm min}) = 1$, since all microhalos within $R_{\rm min}$ are destroyed. Microhalos with a concentration of 1.5 that are tidally stripped to r_s will retain around 60% of their original mass [11], with the mass loss increasing with concentration. Thus, we set $f_s(r > R_{\rm min}) = 1 - 0.6 f_{\rm tot}(z_f)$ and assume constant f_s for $r > R_{\rm min}$ and $r < R_{\rm min}$. We can then write the total host halo boost factor as a sum of the individual contributions:

$$J = J_{\rm micro} + J_{\rm halo}(r < R_{\rm min}) + f_s^2[J_{\rm halo} - J_{\rm halo}(r < R_{\rm min})], \tag{75}$$

where the f_s^2 comes from the fact that J-factors are integrals of density squared. $J_{\rm halo}$ is the volume integral of density squared multipled by a factor of $[1 + B_{\rm std}(M_h)]$, with $B_{\rm std}(M_h)$ the boost-mass relationship for large host halos that form in the absence of an EMDE from Ref. [27]:

$$\begin{aligned} J_{\rm halo} &= [1+B_{\rm std}(M_h)]4\pi\int_0^\infty r^2\bar{\rho}_\chi^2(r)\mathrm{d}r \\ &= [1+B_{\rm std}(M_h)]\frac{f_\chi^2 M_h \rho_{200} c_h^3}{9[\ln(1+c_h)-c_h/(1+c_h)]^2}. \end{aligned} \tag{76}$$

once again with c_h from the mass-concentration relation from Ref. [27], which correctly matches the concentrations of simulated halos in the mass range from $10^{-5}\ M_\odot$ to $10^{15}\ M_\odot$.

Since microhalos are destroyed within $r < R_{\rm min}$ and subhalos with $M > M_{\rm MH}$ are less dense than EMDE-generated microhalos, we expect them to not survive within $R_{\rm min}$ either. Therefore, the J-factor contribution from the host halo within $R_{\rm min}$ is simply the contribution from the smooth NFW profile of the host:

$$\begin{aligned} J_{\rm halo}(r < R_{\rm min}) &= 4\pi\int_0^{R_{\rm min}} r^2\bar{\rho}_\chi^2(r)\mathrm{d}r \\ &= \frac{f_\chi^2 M_h \rho_{200} c_h^3}{3[\ln(1+c_h)-c_h/(1+c_h)]^2}\mathcal{J}\Big(\frac{R_{\rm min}}{R_s}\Big) \end{aligned} \tag{77}$$

where

$$\mathcal{J} \equiv \frac{y^3+3y^2+3y}{3(y+1)^3}. \tag{78}$$

Here, the $\mathcal{J}$ function comes about from only evaluating the integral in Eq. (77) out to $R_{\rm min}$ rather than to infinity. We now find the total boost factor generated by an EMDE of a galaxy-mass host halo by substituting all of the necessary equations into Eq. (75) and dividing by the reference integral $4\pi\int_0^\infty r^2\bar{\rho}_\chi^2(r)\mathrm{d}r$ using a smooth NFW profile for the host halo:

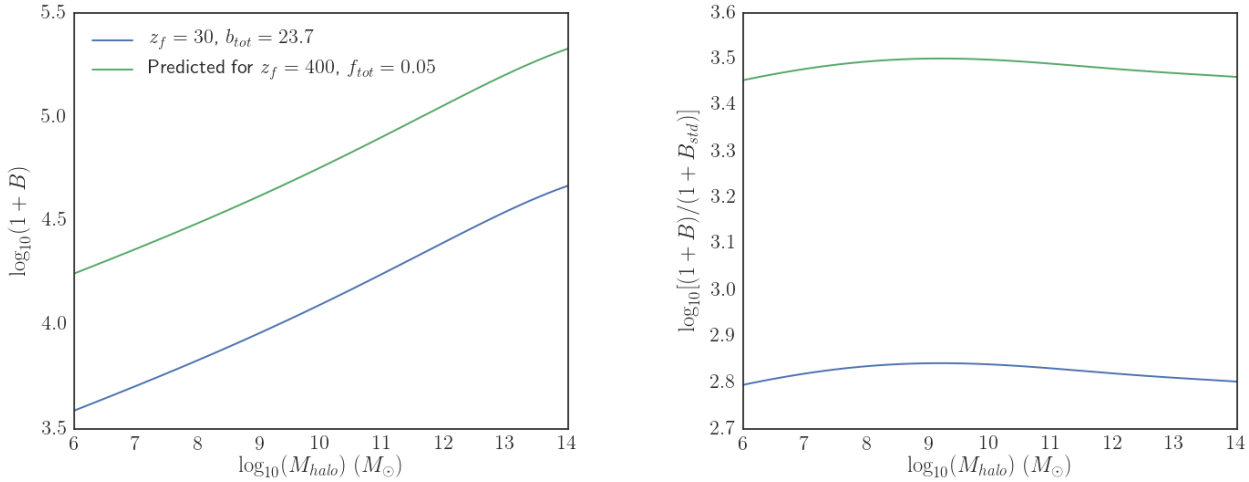

FIG. 28. The total boost factor and relative boost factor generated by an EMDE with $k_{\rm cut}/k_{\rm RH} = 20$. On left: the boost factor as calculated in Eq. (79) with $b_{\rm tot}(z_f = 30)$ determined from $B_s(M_{\rm mh})$ from the $(30\ {\rm pc}/h)^3$ EMDE simulation. The curve is compared to an evaluation at $z_f = 400$ with $b_{\rm tot} = f_{\rm tot} = 0.05$ without a $B_s(M_{\rm mh})$ but assuming that halos formed as early as $z_f = 400$ survive, as done in Ref. [11]. On right: The same boost factors as in the left plot divided by the boost factor from standard subhalos with masses above $10^{-12}\ M_\odot$ [27]. In these figures, we assume that the EMDE-generated microhalos are destroyed within $R_{\rm min} = \sqrt{R_s/(100\ {\rm kpc})}$ kpc.

$$1 + B \gtrsim 36 b_{\rm tot}(z_f)\Big[\frac{\rho_{200}(z_f)}{\rho_{200}}\Big]\Big[\frac{M_h(r > R_{\rm min})}{M_h}\Big]\frac{[\ln(1+c_h) - c_h/(1+c_h)]^2}{c_h^3} + [1 + B_{\rm std}(M_h)]f_s^2 + 3\mathcal{J}\Big(\frac{R_{\rm min}}{R_s}\Big)(1 - f_s^2) \tag{79}$$

Figure 28 demonstrates $1+B$ as a function of the host halo mass M_h compared against the relative boost from an EMDE defined as $(1+B)/(1+B_{\rm std})$. Here, $B_{\rm std}$ from Ref. [27] was evaluated for the boost factor from subhalos with masses larger than $10^{-6}\ M_\odot$ and mass function $dN/dm \propto m^{-2}$ multiplied by a factor of 5/2 to match their boost factor results down to a minimum subhalo mass of $10^{-12}\ M_\odot$. We do this so that the standard boost factors $B_{\rm std}$ account for all subhalos down to the free-streaming cut-off scale in the absence of an EMDE.

We see that the boost factor is significantly dominated by the first term in Eq. (79), with EMDE-generated microhalos being the primary contributor to the boost factor, as expected. Ref. [11] chose an optimistic scenario for $k_{\rm cut}/k_{\rm RH} = 20$ at $z_f = 400$ with $f_{\rm tot}(z_f) = 0.05$ as predicted by the Press-Schecter mass function. Here, the majority of the boost factor is due to the high density that these primordial microhalos form at, but this configuration does not account for additional formation of microhalos at later times as well as the potential destruction of a fraction of the primordial microhalo population. Unfortunately, it seems that the more accurate boost based on our microhalo boost-mass relationship from the cosmological simulations is around a factor of 5 lower than this optimistic boost prediction. Note also that although the more massive host halos have significantly higher boost factors, the relative boost from an EMDE is nearly independent of mass, as shown in the right panel of Fig. 28.

As a final verification, we calculate the relative boost with parameters from the 30 $({\rm pc}/h)^3$ standard simulation, namely $b_{\rm tot}(z_f) = 0.11$ and $f_{\rm tot}(z_f) = 0.025$. We find that the relative boost is nearly constant at $(1+B)/(1+B_{\rm std}) = 4.7$, demonstrating that the boost-mass relationship from Ref. [27] is consistent with the total boost factor as determined with the standard $B_s(M_{\rm mh})$ from our simulations encoded into $b_{\rm tot}(z_f)$. It is not surprising that we find $(1+B)/(1+B_{\rm std}) > 1$ for our standard simulations, as the reference curves used to calculate $b_{\rm tot}(z_f)$ assume a fixed $c = 2$ for the microhalos, whereas $1 + B_{\rm std}$ uses a concentration-mass relationship. Therefore, contributions to the boost in our calculated $1+B$ can be attributed to both substructure and microhalos that have concentrations $c > 2$ with higher smooth densities than their reference curves, whereas boost in $1 + B_{\rm std}$ only comes from substructure.

V. SUMMARY AND DISCUSSION

An EMDE is a general prediction of inflation and high-energy theories. The scalar fields or transient particles typically dominate the cosmic energy density until a rather low reheat temperature on the order of a few

hundred GeV. The delayed reheating due to an EMDE significantly modifies the relationship between dark matter particle properties and the observed relic abundance [30]. The fact that dark matter density perturbations grow linearly with the scale factor during an EMDE has been established for both thermal [11] and non-thermal [5] production mechanisms. Microhalos could potentially provide a powerful probe of the early Universe because they form as the result of these enhanced density perturbations that enter the cosmological horizon before reheating.

The enhancement due to the EMDE is dependent on the ratio between the free-streaming cut-off scale and the reheating scale $k_{\rm cut}/k_{\rm RH}$. The EMDE causes the dark matter annihilation cross-section to decrease, and so we must consider $100 < m_\chi/T_{\rm RH} < 200$ to avoid a cross-section that is suppressed too heavily for a substructure boost to overcome while also keeping dark matter freeze-out during the EMDE. Our analytic model constructed based off of the time evolution of Eq. (12) shows that in order to get $k_{\rm cut}/k_{\rm RH} = 20$, a ratio potentially high enough to produce observable annihilation signatures, the ratio between the temperatures at standard kinetic decoupling and reheating $T_{\rm kdS}/T_{\rm RH} \gtrsim 6$ in order to remain within $100 < m_\chi/T_{\rm RH} < 200$, as indicated by Fig. 11. In most models, dark matter freezes out before it kinetically decouples, and with $T_f/T_{\rm RH} \approx 20$ and $T_{\rm kd}/T_{\rm RH} \approx 54$ for our minimum temperature ratio $T_{\rm kdS}/T_{\rm RH} \gtrsim 6$, the outlook is certainly less than optimistic for detection. Lower temperature ratios that provide $k_{\rm cut}/k_{\rm RH} \gtrsim 20$ are possible, but only for $m_\chi/T_{\rm RH} > 200$, as seen in Fig. 11. Unfortunately, these configurations reduce the annihilation cross section by more than an annihilation boost due to microhalo substructure could possibly compensate.

Moving forward with a $k_{\rm cut}/k_{\rm RH} = 20$, we have determined the fate of the earliest forming microhalos via cosmological simulations. Using `GADGET-2` N-body simulations driven by EMDE-enhanced power spectra, we studied the halo mass functions $dn/d\ln M$, the differential bound-mass fraction $df/d\ln M$, and the total bound fraction $f_{\rm tot}$ of the simulated dark matter structure. We simulated the evolution of multiple box sizes for convergence testing and compared the results of each to standard simulations with power spectra generated with a free-streaming cut-off and the onset of radiation domination immediately after inflation. We studied the numerical density profiles of several microhalos and constructed a smooth reference integral based off of the NFW profile.

With the simulation particle data and dark matter halo catalogs generated by `Rockstar`, we move forward to calculate the dark matter annihilation boost in individual microhalos from the simulation. This is achieved by numerically integrating the density squared of the microhalo in the J-factor and dividing this quantity by the reference integral. After optimizing the resolution of the J-factor integration routine to scale with the number of particles in a given halo, we calculated the boost factor for all host microhalos in each of our simulations studied the microhalo boost-mass relationship $B_s(M_{\rm mh})$. The boosts were partitioned into mass bins and the statistics of each bin were studied. We found very little variance in the boosts for each mass bin, concluding that the majority of the uncertainty in our calculations lies in our J-factor integration resolution. We demonstrate in Fig. 23 that the J-factor grows monotonically with resolution, and we used a fairly conservative resolution in order to place a lower-bound on the total boost factor.

Finally, we calculated the total boost factor for a galaxy-mass host halo based on analytical predictions from Ref. [11]. We compared the total boost factor calculated with a differential bound fraction-averaged boost factor $b_{\rm tot}(z_f)$ based off of our simulations to the boost factor assuming a total bound fraction of $f_{\rm tot}(z_f) = 0.05$ at $z_f = 400$. The total boost factor based on our simulation results is a factor of 5 lower than the prediction for halos that form at $z_f = 400$ and are not destroyed. It is likely that either the microhalos in our simulation have lower densities than previously expected or that more microhalos are destroyed due to tidal stripping than only those within the calculated $R_{\rm min}$ of their host halo.

In a future work, we will complete this analysis by calculating the annihilation detection outlook considering the newly found total boost factors. Ref. [11] finds that a large boost factor of $1 + B \gtrsim 20,000$ is sufficient to compensate for a lowered cross-section, bringing the annihilation rate above current observational thresholds. If an EMDE did indeed boost the dark matter annihilation rate by this factor, detection of annihilation signatures could be possible with missions such as the *Fermi Gammay-Ray Telescope* [14]. If higher resolution simulations demonstrate an increased boost factor due to additional resolved substructure, it is possible that dSph galaxies may indeed have a high enough boost factor for annihilation to be observed. This would only require approximately a factor of 5 increase for $10^6\ M_\odot$ dSph galaxies. It is also possible that our conservative resolutions in the J-factor calculations cause us to underestimate the boost factors by a significant margin. If the total boost factors are indeed fairly accurate as reported and not just strong lower bounds, the next generation of γ-ray telescopes could potentially provide the necessary increase in sensitivity to constrain EMDE scenarios.

[1] A. H. Guth, Phys. Rev. D **23**, 347 (1981).
[2] M. S. Turner, Phys. Rev. D **28**, 1243 (1983).
[3] G. Kane, K. Sinha, and S. Watson, Int. J. Mod. Phys. D **24**, 1530022 (2015), arXiv:1502.07746v1.
[4] G. Coughlan, W. Fischler, E. W. Kolb, S. Raby, and G. Ross, Physics Letters B **131**, 59 (1983).

[5] A. L. Erickcek and K. Sigurdson, Phys. Rev. D **84**, 1 (2011), arXiv:1106.0536.

[6] S. Hannestad, Phys. Rev. D **70** (2004), arXiv:0403291.

[7] K. Ichikawa, M. Kawasaki, and F. Takahashi, Phys. Rev. **D72**, 043522 (2005), arXiv:astro-ph/0505395 [astro-ph].

[8] J. S. Bullock, T. S. Kolatt, Y. Sigad, R. S. Somerville, A. V. Kravtsov, A. A. Klypin, J. R. Primack, and A. Dekel, Mon. Not. Roy. Astron. Soc. **321**, 559 (2001), arXiv:astro-ph/9908159 [astro-ph].

[9] R. H. Wechsler, J. S. Bullock, J. R. Primack, A. V. Kravtsov, and A. Dekel, Astrophys. J. **568**, 52 (2002), arXiv:astro-ph/0108151 [astro-ph].

[10] A. V. Maccio', A. A. Dutton, and F. C. v. d. Bosch, Mon. Not. Roy. Astron. Soc. **391**, 1940 (2008), arXiv:0805.1926 [astro-ph].

[11] A. L. Erickcek, Phys. Rev. D **92** (2015), arXiv:1504.03335.

[12] Planck Collaboration, A & A **594**, A13 (2016), arXiv:1502.01589.

[13] V. Springel, Mon. Not. R. Astron. Soc. **364**, 1105 (2005), astro-ph/0505010.

[14] Fermi-LAT Collaboration, Phys. Rev. Lett. **115**, 231301 (2015), arXiv:1503.02641 [astro-ph.HE].

[15] E. Bertschinger, Phys. Rev. D **74** (2006), 10.1103/PhysRevD.74.063509, arXiv:0607319 [astro-ph].

[16] P. S. Behroozi, R. H. Wechsler, and H.-Y. Wu, Astrophys. J. **762**, 109 (2013), arXiv:1110.4372.

[17] R. K. Sheth and G. Tormen, Mon. Not. R. Astron. Soc. **308**, 119 (1999), astro-ph/9901122.

[18] W. H. Press and P. Schechter, Astrophys. J. **187**, 425 (1974).

[19] J. F. Navarro, C. S. Frenk, and S. D. M. White, Astrophys. J. **462**, 563 (1996), astro-ph/9508025.

[20] G. B. Gelmini and P. Gondolo, JCAP **0810**, 002 (2008), arXiv:0803.2349 [astro-ph].

[21] I. R. Waldstein, A. L. Erickcek, and C. Ilie, arXiv E-Prints (2016), arXiv:1609.05927.

[22] W. Hu and N. Sugiyama, Astrophys. J. **471**, 542 (1996), arXiv:astro-ph/9510117 [astro-ph].

[23] L. Visinelli and P. Gondolo, Phys. Rev. **D91**, 083526 (2015), arXiv:1501.02233 [astro-ph.CO].

[24] P. Ramachandran and G. Varoquaux, Computing in Science & Engineering **13**, 40 (2011).

[25] D. Anderhalden and J. Diemand, J. Cosmol. Astropart. Phys. **4**, 009 (2013), arXiv:1302.0003.

[26] T. Ishiyama, Astrophys. J. **788**, 27 (2014), arXiv:1404.1650 [astro-ph.CO].

[27] M. A. Sánchez-Conde and F. Prada, Mon. Not. R. Astron. Soc. **442**, 2271 (2014), arXiv:arXiv:1312.1729v3.

[28] F. Pedregosa, G. Varoquaux, A. Gramfort, V. Michel, B. Thirion, O. Grisel, M. Blondel, P. Prettenhofer, R. Weiss, V. Dubourg, J. Vanderplas, A. Passos, D. Cournapeau, M. Brucher, M. Perrot, and E. Duchesnay, Journal of Machine Learning Research **12**, 2825 (2011).

[29] E. Hayashi, J. F. Navarro, J. E. Taylor, J. Stadel, and T. R. Quinn, Astrophys. J. **584**, 541 (2003), arXiv:astro-ph/0203004 [astro-ph].

[30] M. Kamionkowski and M. S. Turner, Phys. Rev. D **42**, 3310 (1990).